

Molecular gas and star formation in nearby starburst galaxy mergers

HAO HE,¹ CONNOR BOTTRELL,² CHRISTINE WILSON,¹ JORGE MORENO,³ BLAKESLEY BURKHART,^{4,5}
 CHRISTOPHER C. HAYWARD,⁵ LARS HERNQUIST,⁶ AND ANGELA TWUM³

¹*McMaster University*

1280 Main St W, Hamilton, ON L8S 4L8, CAN

²*Kavli Institute for the Physics and Mathematics of the Universe (WPI), UTIAS, University of Tokyo
 Kashiwa, Chiba 277-8583, Japan*

³*Department of Physics and Astronomy, Pomona College,
 Claremont, CA 91711, USA*

⁴*Department of Physics and Astronomy, Rutgers University,
 136 Frelinghuysen Rd., Piscataway, NJ 08854, USA*

⁵*Center for Computational Astrophysics, Flatiron Institute,
 162 Fifth Avenue, New York, NY 10010, USA*

⁶*Center for Astrophysics, Harvard & Smithsonian,
 60 Garden Street, Cambridge, MA 02138, USA*

(Received February 1, 2023; Revised xxx; Accepted xxx)

Submitted to ApJ Letter

ABSTRACT

We employ the Feedback In Realistic Environments (FIRE-2) physics model to study how the properties of giant molecular clouds (GMCs) evolve during galaxy mergers. We conduct a pixel-by-pixel analysis of molecular gas properties in both the simulated control galaxies and galaxy major mergers. The simulated GMC-pixels in the control galaxies follow a similar trend in a diagram of velocity dispersion (σ_v) versus gas surface density (Σ_{mol}) to the one observed in local spiral galaxies in the Physics at High Angular resolution in Nearby Galaxies (PHANGS) survey. For GMC-pixels in simulated mergers, we see a significant increase of factor of 5 – 10 in both Σ_{mol} and σ_v , which puts these pixels above the trend of PHANGS galaxies in the σ_v vs Σ_{mol} diagram. This deviation may indicate that GMCs in the simulated mergers are much less gravitationally bound compared with simulated control galaxies with virial parameter (α_{vir}) reaching 10 – 100. Furthermore, we find that the increase in α_{vir} happens at the same time as the increase in global star formation rate (SFR), which suggests stellar feedback is responsible for dispersing the gas. We also find that the gas depletion time is significantly lower for high α_{vir} GMCs during a starburst event. This is in contrast to the simple physical picture that low α_{vir} GMCs are easier to collapse and form stars on shorter depletion times. This might suggest that some other physical mechanisms besides self-gravity are helping the GMCs in starbursting mergers collapse and form stars.

Keywords: ISM: clouds, ISM: kinematics and dynamics, ISM: structure, galaxies: interactions, galaxies: starburst, galaxies: star formation

1. INTRODUCTION

Despite the diversity of galaxy morphology and environment, giant molecular clouds (GMCs) are the sites of star formation across cosmic time (Krumholz et al. 2019; Chevance et al. 2020). As one of the most promising star formation model, the turbulence model (Krumholz & McKee 2005; Hennebelle & Chabrier 2011) suggest a

relatively uniform star formation efficiency per freefall time (ϵ_{ff}) for individual GMCs. They predict that the observed scatter in ϵ_{ff} could be accounted for by the diversity in GMC properties (e.g. virial parameter α_{vir} and Mach number). However, Lee et al. (2016) show that the observed scatter is larger than these early theoretical predictions expected and updated models suggest that cloud evolution, in addition to initial conditions such as Mach number and α_{vir} , should be accounted for (see Burkhart 2018; Mocz & Burkhart 2018; Burkhart & Mocz 2019). Furthermore, Grudić et al. (2018) show in their simulation that GMCs in starburst galaxies can have different ϵ_{ff} in normal spiral galaxies. Hence, to understand the links between GMCs and star formation in galaxies, it is essential to study various GMC properties in a broad range of environments.

However, modeling of GMCs starting from the scales of galaxies and cosmological zoom-ins is complicated by challenges in capturing the structure of the coldest and densest gas, which is heavily affected by various numerical choices, such as resolution (e.g. Bournaud et al. 2008; Teyssier et al. 2010) and the treatment of feedback (Fall et al. 2010; Murray et al. 2010; Dale et al. 2014; Myers et al. 2014; Raskutti et al. 2016; Kim et al. 2017; Grudić et al. 2018; Smith et al. 2021). Most resolved GMC simulations focus on the evolution of individual GMCs (e.g. Burkhart et al. 2015; Howard et al. 2018; Li et al. 2019; Decataldo et al. 2020; Burkhart et al. 2020) and ignore the wider environment. Only a handful of galaxy simulations have the ability to model GMC populations inside Milky-Way-like galaxies (Jeffreson & Kruijssen 2018; Benincasa et al. 2020) and mergers (Renaud et al. 2019a; Li et al. 2022).

High-resolution CO observations have successfully characterized GMCs in the Milky Way (e.g. Rice et al. 2016; Rico-Villas et al. 2020; Miville-Deschênes et al. 2017; Colombo et al. 2019; Lada & Dame 2020) and nearby galaxies (e.g. Donovan Meyer et al. 2013; Hughes et al. 2013; Colombo et al. 2014; Leroy et al. 2016; Schruba et al. 2019). In particular, the recently completed PHANGS-ALMA survey (Leroy et al. 2021) has expanded these observations across a complete sample of nearby spiral galaxies, providing direct measurements of molecular gas surface density Σ_{mol} , velocity dispersion σ_v and size of GMCs, which are key quantities for determining the physical state of GMCs (Larson 1981). Observations show that the correlation between σ_v^2/R and Σ_{mol} is nearly linear (e.g., Heyer & Dame 2015; Sun et al. 2018, 2020), which is consistent with the theoretical prediction that most clouds follows the Larson’s second law (Larson 1981), which indicates a constant ratio between clouds’ kinetic energy and gravitational poten-

tial energy. This universal correlation provides us with a starting point to study how other galactic environmental factors (e.g., external pressure, stellar potential) influence the dynamical state of GMCs.

Unlike studies targeting isolated galaxies, GMCs in starburst galaxy mergers are less well studied. On the observational side, the scarcity of nearby mergers means that we have only a handful of systems with GMC resolution data (Wei et al. 2012; Ueda et al. 2012; Whitmore et al. 2014; Elmegreen et al. 2017; Brunetti et al. 2020; Brunetti 2022; Sánchez-García et al. 2022; Bellocchi et al. 2022). These studies show that GMCs in mergers have significantly higher gas surface densities and are less gravitationally bound compared to GMCs in normal spirals. However, it is difficult to draw statistically robust conclusions on how GMC properties evolve across various merging stages based on these limited number of local galaxy mergers. On the simulation front, only a handful of studies (e.g., Teyssier et al. 2010; Renaud et al. 2014; Fensch et al. 2017) have the ability to probe the cold gas at $\sim\text{pc}$ scale starting from cosmological scales. Using a comprehensive library of idealized galaxy merger simulations based on the FIRE-2 physics model, Moreno et al. (2019) show that SFR enhancement is accompanied by an increase in the cold dense gas reservoir. This simulation suite thus provides us with the ideal tool to properly examine GMC evolution along the entire merging sequence.

This paper explores how GMC properties evolve during the starburst merging event using the FIRE-2 merger suite from Moreno et al. (2019) and performs comparisons with observations to test the simulation model. In Section 2, we describe this simulation suite and the observational data used for comparison. Section 3 compares the $\sigma_v - \Sigma_{\text{mol}}$ relation between control simulated galaxies and normal spirals in the PHANGS-ALMA sample. Section 4 examines the $\sigma_v - \Sigma_{\text{mol}}$ relation for mergers in both observations and simulations. In Section 5, we discuss and interpret various aspects of the comparison between observations and simulations.

2. DATA PROCESSING

2.1. Simulated data

2.1.1. The FIRE-2 Model

We use the FIRE-2 model (Hopkins et al. 2018), which employs the hydrodynamic code GIZMO (Hopkins 2015, 2017). Compared with the previous version, FIRE-2 adopts the updated meshless finite-mass (MFM) magnetohydrodynamics (MHD) solver, which is designed to capture the advantages of both grid-based and particle-based methods. We refer the reader to Hopkins (2015) and Hopkins et al. (2018) for details. The model includes

treatment of radiative heating and cooling from free-free, photo-ionization/recombination, Compton, photo-electric, dust-collisional, cosmic ray, molecular, metal line, and fine-structure processes. Star formation occurs in gas that is self-gravitating ($3D \alpha_{\text{vir}} < 1$ at the resolution scale), self-shielded, and denser than 1000 cm^{-3} (see Appendix C of Hopkins et al. 2018). Stellar feedback mechanisms include (i) mass, metal, energy, and momentum flux from supernovae type Ia & II; (ii) continuous stellar mass-loss through OB/AGB winds; (iii) photoionization and photoelectric heating; and (iv) radiation pressure. Each stellar particle is treated as a single stellar population. Mass, age, metallicity, luminosity, energy, mass-loss rate, and stellar feedback event rate for each stellar particle are calculated using the STARBURST99 stellar population synthesis model (Leitherer et al. 1999). The model does not account for feedback generated via accretion of gas onto a supermassive black hole (SMBH).

2.1.2. Our FIRE-2 galaxy suite

Moreno et al. (2019) present a suite of idealized galaxy merger simulations (Initial conditions are manually set instead of from cosmological simulations; see also Bottrell et al. 2019; Moreno et al. 2021; McElroy et al. 2022) covering a range of orbital parameters and mass ratios between 4 disc galaxies (G1, G2, G3 and G4, in order of increasing total stellar mass of (0.21, 1.24, 2.97 and $5.5 \times 10^{10} M_{\odot}$), along with separate runs for each disk galaxy in isolation (the control runs). Their orbit settings contain 3 orbital spin directions, 3 impact parameters and 3 impact velocities (see Fig. 3 in Moreno et al. 2019). For these simulations, the highest gas density and spatial resolution are $5.8 \times 10^5 \text{ cm}^{-3}$ and 1.1 pc, respectively. The gravitational softening lengths are 10 pc for the dark matter and stellar components and 1 pc for the gaseous component. The mass resolution for a gas particle is $1.4 \times 10^4 M_{\odot}$. The time resolution of a typical snapshot is 5 Myr (See further details in Moreno et al. 2019).

Table 1. Orbital Parameter of ‘e1’ and ‘e2’ orbit

	e1	e2
Apo. Dist. (kpc) ^a	60	120
Peri. Dist. (kpc) ^a	15.5	9.3

^a First apocentric distance between the centers of two galaxies.

^b Second pericentric distance between the centers of two galaxies.

For our analysis, we focus on the simulation run of isolated G2 and G3 galaxies along with one of G2&G3

merger suites. The detailed information of G2 and G3 galaxies is in Moreno et al. (2019, Table 2). The G2&G3 merger suites have a mass ratio of 1:2.5 and hence are similar to major mergers such as the Antennae and NGC 3256 for which we have observational data. In addition, G2 and G3 have stellar masses within the range of the PHANGS sample (10^{10} – $10^{11} M_{\odot}$; Leroy et al. 2021). We choose the ‘e’ orbit (Robertson et al. 2006, roughly prograde), which is expected to maximally enhance the star formation rate. In most of our analyses, we focus on the ‘e2’ orbit since this is the fiducial run in Moreno et al. (2019). We use the ‘e1’ orbit as a comparison in some cases as it has smaller impact parameter and is more similar to the orbit of the Antennae merger (Privon et al. 2013), for which we have GMC observational data. The pericentric distance of ‘e1’ and ‘e2’ orbit is listed in Table 1.

2.1.3. Molecular gas

We follow the scheme in Moreno et al. (2019) to separate the ISM of our simulated galaxy mergers into 4 components based on temperature and density: hot, warm, cool, and cold-dense gas, which roughly correspond to the hot, ionized, atomic, and molecular gas in observations (see Table 4 in Moreno et al. 2019). The components that are most important for this work are the cool (temperatures below 8000 K and densities above 0.1 cm^{-3}) and the cold-dense gas (temperatures below 300 K and densities above 10 cm^{-3}), which corresponds to H I and H₂. This choice captures HI and H₂ gas reasonably well (Orr et al. 2018). Orr et al. (2018) also demonstrate that using this threshold to separate H₂ and HI yields reasonable agreement with the observed Kennicutt-Schmidt law (Kennicutt 1998; Kennicutt & Evans 2012). In the following, we refer to total gas as the sum of the gas in the cool and cold-dense phases (simulations) or in the atomic and molecular phases (observations).

We adopt the same definition of molecular gas as in Moreno et al. (2019) (temperature below 300 K and density above 10 cm^{-3}). Guszejnov et al. (2017) demonstrate that the model successfully reproduces the GMC mass function in the Milky Way (Rice et al. 2016) and the size-linewidth relation (e.g., the Larson scaling relationship, Larson 1981) in our Galaxy (Heyer et al. 2009; Heyer & Dame 2015) and in nearby galaxies (Bolatto et al. 2008; Fukui et al. 2008; Muraoka et al. 2009; Roman-Duval et al. 2010; Colombo et al. 2014; Tosaki et al. 2017). Given the density cut of 10 cm^{-3} and mass resolution of $1.4 \times 10^4 M_{\odot}$, the lower limit of our spatial resolution ($\sqrt[3]{M/\rho}$, where M is the mass resolution and ρ is the mass volume density) is ~ 40 pc, which

is smaller than the typical scale of observed GMCs (40 – 100 pc, [Rosolowsky et al. 2021](#)). In addition, GMC mass function peaks at $10^5 - 10^6 M_\odot$ in Milky Way ([Rice et al. 2016](#)), which is significantly larger than our mass resolution. Therefore, we would generally expect more than 1 gas particle is included for molecular gas in each GMC-scale pixel.

For generating different components of the ISM, the simulations start with a homogeneous ISM with a temperature of 10^4 K and solar metallicity. The multi-phase ISM then emerges quickly as a result of cooling and feedback from star formation. The initial gas mass for the simulation is set to match the median HI mass from the xCOLDGASS survey ([Catinella et al. 2018](#)).

2.1.4. Data cubes

We first convert the FIRE-2 molecular gas data into mass-weighted position-position-velocity (p-p-v) data cubes to match the format of the CO data from radio observations ([McMullin et al. 2007](#)). We adopt the cube construction method created for [Bottrell et al. \(2022\)](#) and [Bottrell & Hani \(2022\)](#) and then adapted to the FIRE-2 merger suite by [McElroy et al. \(2022\)](#). Kinematic cubes are produced along four lines-of-sight (labeled as ‘v0’, ‘v1’, ‘v2’, ‘v3’), defined by the vertices of a tetrahedron centered at the primary galaxy (G3 in this work). For the isolated galaxy simulations, we generate p-p-v data cubes at different inclination angles (10 – 80 degrees). We adopt a pixel size of 100 pc and velocity resolution of 2 km s^{-1} , which is similar to PHANGS choice ([Sun et al. 2020](#)). The field of view (FOV) for the data cube is set to be 25 kpc.

Then we create zeroth-moment maps of the gas surface density Σ_{mol} and second-moment maps of the velocity dispersion σ_v . We do not set any thresholds on these moment maps since we argue that every gas particle in the simulated cube should be treated as a real signal, rather than observational noise. However, in later analyses, when we display σ_v versus Σ_{mol} for the simulated data, we select pixels with Σ_{mol} greater than $1 M_\odot \text{ pc}^{-2}$, which approximates the lower limit of the molecular gas detection threshold in the observational data ([Sun et al. 2018](#)). We also exclude pixels detected in fewer than two velocity channels in the simulated cube to exclude inaccurate measurements of σ_v .

To characterize clouds, we use a pixel-based analysis ([Leroy et al. 2016](#)), which treats each pixel as an individual GMC, rather than identifying each individual cloud from the data cube. This approach has been widely applied to GMC analyses for PHANGS galaxies ([Sun et al. 2018, 2020](#)). Compared to the traditional cube-based approach, this new method requires

minimal assumptions and can be easily applied to many datasets in a uniform way, while still giving us the essential GMC properties (e.g., molecular gas surface density Σ_{mol} , gas velocity dispersion σ_v). On the other hand, the pixel-based method has a major disadvantage of not able to decompose different cloud components along the same line of sight. Several observational studies (e.g. [Brunetti & Wilson 2022](#); [Sun et al. 2022](#)) have compared this new approach with the traditional approach and found good agreement on cloud properties between two methods for both normal spiral galaxies and starburst mergers, especially for clouds in galaxy disks. These comparisons show pixel-based analysis should be valid for capturing individual cloud properties, especially for galaxy disks which generally have single-layer of GMCs (see Section 5.1 for detailed discussion about the projection effect). In this work, we adopt this approach to match the method in [Brunetti et al. \(2020\)](#) and [Brunetti \(2022\)](#). We also note that since we treat each pixel as a GMC, these GMCs do not necessarily represent independent ISM structures. In fact, given the mass resolution of $1.4 \times 10^4 M_\odot$, we can barely resolve the internal structure of most massive GMCs of $\sim 10^6 M_\odot$ (100 elements). We refer to them as GMCs in this paper to be consistent with similar observational analyses (e.g. [Sun et al. 2018, 2020](#)).

2.2. Star Formation Rate Maps

To further explore how the GMC properties at 100 pc scale affect the star formation, we also make SFR maps with the same resolution of 100 pc for the simulated mergers at different times. We create these maps using a method similar to the one used to create the gas cubes. We include all the stellar particles with age younger than 10 Myr and create p-p-v data cubes for these stellar particles. The mass-weighted cubes are integrated along the velocity axis to produce 2D maps of stellar mass formed within the last 10 Myr. These surface-density mass maps are subsequently divided by 10 Myr to obtain the average star-formation rates over the last 10 Myr.

2.3. Observational Data

We use several sets of observations for comparison with our simulations.

2.3.1. Spiral galaxies: PHANGS data

For isolated galaxies, we mainly use the PHANGS data from [Sun et al. \(2020\)](#) with resolution of 90 pc, which is comparable to our pixel size choice of 100 pc. [Sun et al. \(2020\)](#) apply the pixel-based method for statistical analyses of GMC properties for 70 galaxies in the PHANGS sample. We also include GMC data for

M31 from Sun et al. (2018) at resolution of 120 pc. M31 is identified as a green-valley galaxy, similar to our own Milky Way, and hence has a lower total gas fraction than normal spiral galaxies (Mutch et al. 2011). Both M31 and the Milky Way seem to be in a transition from blue spiral galaxies to quenched galaxies via depletion of their cold gas (Bland-Hawthorn & Gerhard 2016). M31 has stellar mass of $10^{11} M_{\odot}$ (Sick et al. 2015), H_2 mass of $3.6 \times 10^8 M_{\odot}$ and HI mass of $4.8 \times 10^9 M_{\odot}$ (Nieten et al. 2006).

2.3.2. Galaxy mergers: the Antennae and NGC 3256

Table 2. Information about the observed mergers in this work

	Antennae	NGC 3256	#References
M_{\star} ($10^{10} M_{\odot}$) ^a	4.5	11.4	(1); (2)
M_{mol} ($10^{10} M_{\odot}$) ^b	1.2	0.8	(3); this work
SFR ($M_{\odot}\text{yr}^{-1}$)	8.5	50	(1); (4)
Sep. (kpc) ^c	7.3	1.1	(5); (4)
t_{now} (Myr) ^d	40	...	(6)
mass ratio ^f	1:1	...	(6)
Peri. Sep (kpc) ^g	10.4	...	(6)

Notes: *a.* Stellar mass. *b.* Molecular gas mass. *c.* Current separation between two nuclei. *d.* Current time since the second passage. *e.* Mass ratio of the two progenitor galaxies. *g.* Pericentric distance of two nuclei from the simulation model. References: (1) Seillé et al. (2022) (2) Howell et al. (2010) (3) Wilson et al. (2000) (4) Sakamoto et al. (2014) (5) Zhang et al. (2001) (6) Karl et al. (2010)

We use the CO 2-1 data for NGC 3256 (Brunetti et al. 2020) and the Antennae (Brunetti (2022, Brunetti et al. in prep)) at resolutions of 90 and 80 pc, respectively. The GMC measurements use the same pixel-based approach as in Sun et al. (2018, 2020). Both NGC 3256 and the Antennae are identified as late-stage major mergers that have been through their second perigalactic passage (Privon et al. 2013). NGC 3256 has stellar mass of $1.1 \times 10^{11} M_{\odot}$, total molecular gas of $8 \times 10^{19} M_{\odot}$ (calculated based on CO 2-1 map in Brunetti & Wilson (2022), assuming α_{CO} of $1.1 M_{\odot} (\text{K km s}^{-1} \text{pc}^2)^{-1}$ and CO 2-1/1-0 ratio of 0.8) and SFR of $50 M_{\odot}\text{yr}^{-1}$ (Sakamoto et al. 2014). In contrast, the Antennae has a stellar mass of $4.5 \times 10^{10} M_{\odot}$ and SFR of $8.5 M_{\odot}\text{yr}^{-1}$ (Seillé et al. 2022). NGC 3256 currently has a more intense starburst, perhaps because it is at different evolutionary stage in the merging process. The detailed information is in Table 2.

To convert the CO 2-1 emission to molecular gas mass requires the assumption of a CO-to- H_2 conversion factor (α_{CO}). The exact value of α_{CO} has large uncertainties

and varies significantly among different types of galaxies, especially for starburst galaxies. Downes & Solomon (1998) find that for starburst U/LIRGs, the α_{CO} value is generally 4 times smaller than that in our Milky Way. The major method for direct measurement of α_{CO} is through large velocity gradient (LVG) radiative transfer modeling of multiple CO and its isotope lines. For α_{CO} in the Antennae, various LVG modeling (e.g. Zhu et al. 2003; Schirm et al. 2014) suggests that the Antennae has α_{CO} close to the Milky Way value of $4.3 M_{\odot} (\text{K km s}^{-1} \text{pc}^2)^{-1}$. This is also supported by the galaxy simulation that specifically matches the Antennae (Renaud et al. 2019a). For NGC 3256, we do not have a direct measurement of α_{CO} . We therefore adopt the treatment from Sargent et al. (2014) to determine the α_{CO} for an individual galaxy as

$$\alpha_{\text{CO}} = (1 - f_{\text{SB}}) \times \alpha_{\text{CO,MS}} + f_{\text{SB}} \times \alpha_{\text{CO,SB}}, \quad (1)$$

where $\alpha_{\text{CO,MS}}$ and $\alpha_{\text{CO,SB}}$ are the conversion factors for the Milky Way ($4.3 M_{\odot} (\text{K km s}^{-1} \text{pc}^2)^{-1}$) and U/LIRGs ($1.1 M_{\odot} (\text{K km s}^{-1} \text{pc}^2)^{-1}$, including helium), and f_{SB} is the probability for a galaxy to be a starburst galaxy, which is determined by its deviation from the star-forming main sequence. We adopt the star-forming main sequence relation from Catinella et al. (2018),

$$\log \text{sSFR}_{\text{MS}} = -0.344(\log M_{\star} - 9) - 9.822, \quad (2)$$

where $\text{sSFR} = \text{SFR} / M_{\star}$ is the specific star formation rate. NGC 3256 has an $\text{sSFR}/\text{sSFR}_{\text{MS}}$ ratio of 15 (Brunetti et al. 2020), which suggests NGC 3256 should have α_{CO} close to the U/LIRG value of $1.1 M_{\odot} (\text{K km s}^{-1} \text{pc}^2)^{-1}$. Therefore, in the following analyses, we will adopt α_{CO} of $4.3 M_{\odot} (\text{K km s}^{-1} \text{pc}^2)^{-1}$ for the Antennae and $1.1 M_{\odot} (\text{K km s}^{-1} \text{pc}^2)^{-1}$ for NGC 3256.

3. CONTROL (ISOLATED) GALAXIES

To test if the simulation successfully reproduces observed GMCs, Figure 1 shows the well-known correlation between σ_v and Σ_{mol} for isolated simulated galaxies and PHANGS-ALMA spiral galaxies. We show σ_v versus Σ_{mol} contours for G2 and G3 galaxies at an inclination angle of 30 degrees, compared with that of observed galaxies. The two simulated galaxies exhibit similar properties (black and dark red solid contours) and generally lie on the trend followed by the PHANGS galaxies. We also plot a red dashed line indicating GMCs with constant virial parameter α_{vir} of 3.1. For the pixel-based

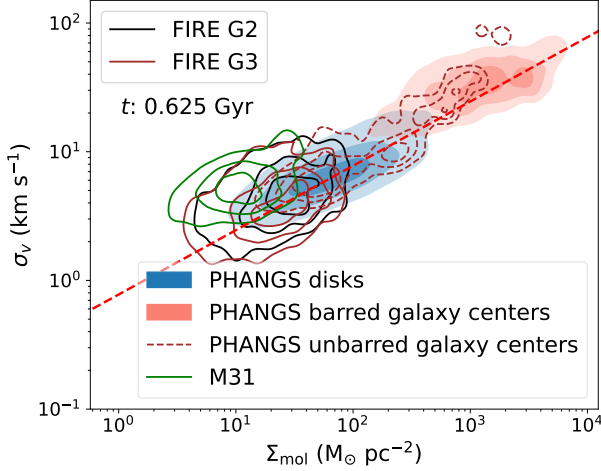


Figure 1. Velocity dispersion versus gas surface density for the G2 (black solid contour) and G3 (brown solid contour) simulated galaxies at 0.625 Gyr with inclination angle of 30 degrees compared to the PHANGS galaxy sample. The contours are mass-weighted and set to include 20%, 50% and 80% of the data. The density contours of PHANGS galaxies (Sun et al. 2020) show the distribution of measurements in galaxy disks (blue shaded contours), the centers of barred galaxies (salmon shaded contours) and the centers of unbarred galaxies (brown dashed contours) with a resolution of 90 pc. The red dashed line marks the position of the median values of α_{vir} for PHANGS galaxies of 3.1 (Sun et al. 2020). We also show the data for M31 (green solid contour) at 120 pc resolution from Sun et al. (2018). We can see that the FIRE-2 spiral galaxies follow the same σ_v - Σ_{mol} relation as the PHANGS galaxies.

analysis, α_{vir} is calculated as (Sun et al. 2018)

$$\begin{aligned} \alpha_{\text{vir}} &= \frac{9 \ln 2}{2\pi G} \frac{\sigma_v^2}{\Sigma_{\text{mol}} R} \\ &= 5.77 \left(\frac{\sigma_v}{\text{km s}^{-1}} \right)^2 \left(\frac{\Sigma_{\text{mol}}}{\text{M}_{\odot} \text{ pc}^{-2}} \right)^{-1} \left(\frac{R}{40 \text{ pc}} \right)^{-1}, \end{aligned} \quad (3)$$

where R is the GMC radius. In Sun et al. (2018), R is set to be the radius of the beam in the image, as each beam is treated as an independent GMC. We can see both our simulated galaxies and observed PHANGS galaxies follow the trend of the constant α_{vir} , which yields the relation of $\sigma_v^2 \propto \Sigma_{\text{mol}}$ that suggests the simulations reproduce GMCs similar to the observations. However, we can see that the two galaxies lie at the low surface-density end of the PHANGS distribution and thus their gas properties are more similar to those of M31 than a typical PHANGS galaxy. Indeed, the molecular and total gas properties of the simulated galaxies are similar to those of M 31, perhaps due to the choice of initial gas mass in the simulations (see Appendix B).

4. MERGING GALAXIES

4.1. GMC linewidth and surface density

We performed a similar σ_v versus Σ_{mol} analysis for our suite of galaxy merger simulations. Since we are particularly interested in how the starburst activity influences GMC properties, we focus on the period right before and after the second passage where we can see the largest contrast in SFR. In Fig. 2 we show some example snapshots of σ_v versus Σ_{mol} for different merger stages during the second passage, along with Σ_{mol} and α_{vir} maps at each snapshot. Note that the datacube is centered on the primary galaxy G3. At the time of first snapshot (2.54 Gyr), right before the start of the second perigalactic passage, the simulated mergers still have Σ_{mol} and σ_v that are similar the isolated galaxies. Then the molecular gas quickly transitions to a more turbulent state with much higher σ_v after the second passage along with a dramatic increase in global SFR, as shown in the snapshot for 2.66 Gyr (middle panel of Fig. 2). The merger at this time still shows two separate nuclei in the zeroth moment map; this is similar to our observed mergers, the Antennae and NGC 3256. At this time, the σ_v versus Σ_{mol} contours for the simulated merger lie above the trend seen for the PHANGS galaxies, similar to NGC 3256, but in contrast to the Antennae, which still lies along the trend of the PHANGS galaxies. The larger deviation above the PHANGS trend implies higher α_{vir} . We note that different α_{CO} choices will affect the position of the contours. If we choose the ULIRG α_{CO} instead of the Milky Way value, the Antennae would have α_{vir} similar to that of NGC 3256 and our G2&G3 merger. The uncertainty in the correct α_{CO} value to use makes it difficult to interpret the data for the Antennae in this context.

The bottom panel of Fig. 2 shows the snapshot at 2.87 Gyr, which marks the post-merger stage after the final coalescence of two nuclei (defined here as the time at which the two central supermassive black holes are at a distance of 500 pc for the last time). This is the time when both Σ_{mol} and σ_v reach their highest values. We can see that most of the molecular gas is concentrated in the central 1 kpc region, with Σ_{mol} reaching $1000 \text{ M}_{\odot} \text{ pc}^{-2}$. σ_v reaches 200 km s^{-1} , which is even higher than the σ_v observed in NGC 3256, which is in an earlier merging stage when the two nuclei have not yet coalesced.

To better quantify the variation of Σ_{mol} and σ_v during the second passage, we plot the 16th, 50th and 84th percentile of the mass-weighted values for all pixels of each snapshot during the second passage in Fig. 3. We also normalize both the median Σ_{mol} and σ_v to the median

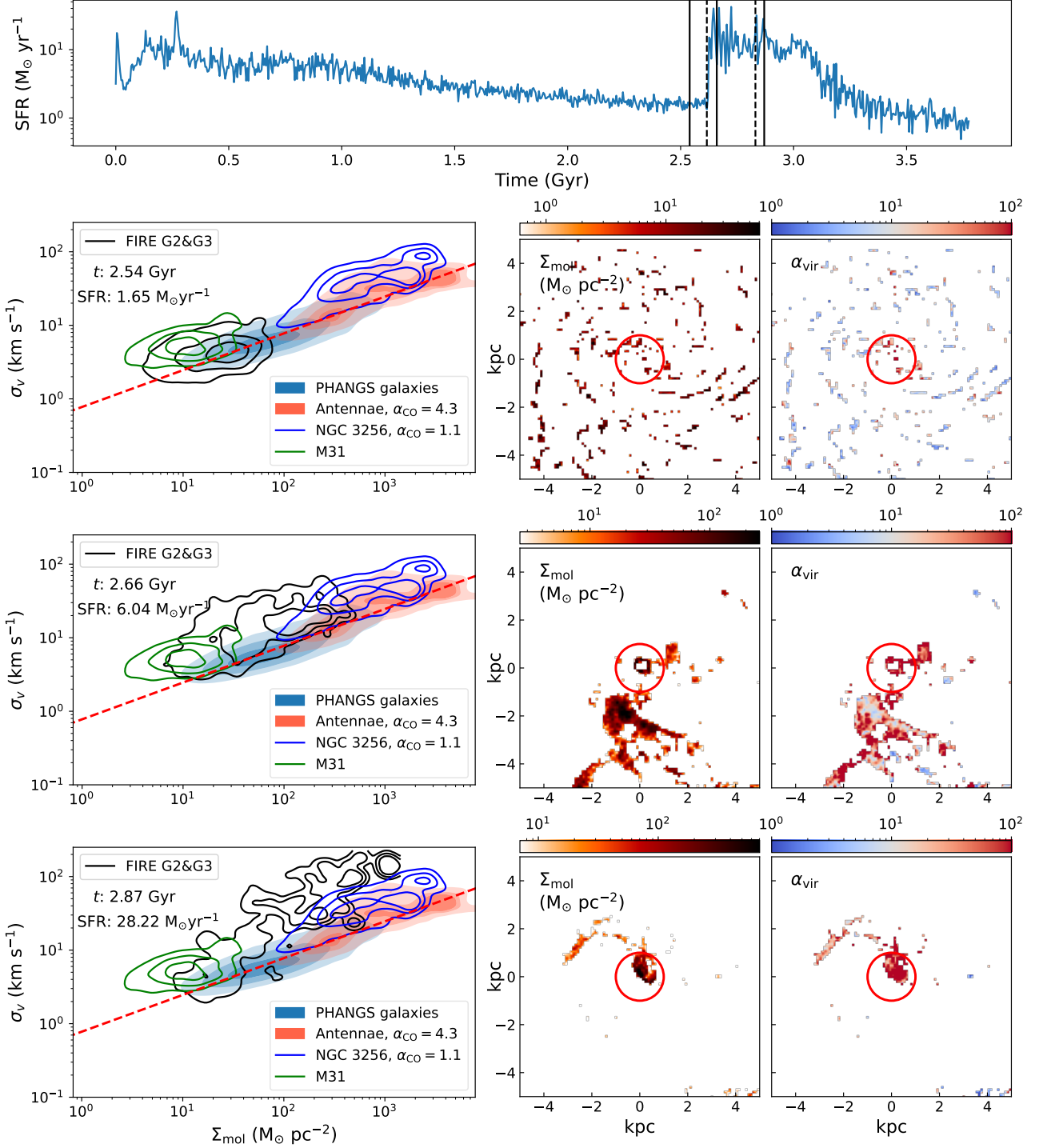


Figure 2. (Top) SFR history for the G2&G3 merger with ‘e2’ orbit with viewing angle of ‘v0’. The 3 solid black vertical lines indicate the time for each snapshot displayed below. The two dashed lines indicate the times at the start of second merging and the final coalesce of two nuclei. (Bottom) Three snapshots. For each snapshot, the left panel shows the σ_v versus Σ_{mol} mass-weighted contour with the same setting as Fig. 1. We also show the density contours for the PHANGS galaxies (filled blue region), NGC 3256 (blue contours) and the Antennae (orange shaded region). For NGC 3256, Σ_{mol} is calculated using the ULIRG α_{CO} of $1.1 M_{\odot} (\text{K km s}^{-1} \text{ pc}^2)^{-1}$. For the Antennae, the gas surface density is calculated using the Milky Way α_{CO} of $4.3 M_{\odot} (\text{K km s}^{-1} \text{ pc}^2)^{-1}$. The red dashed line indicate the line of constant α_{vir} of 3.1. The right two panels show the Σ_{mol} and α_{vir} maps of inner 5 kpc regions where we have most of our detected pixels. The interactive version of the animation is available at https://htmlpreview.github.io/?https://github.com/heh15/merger_animations/blob/main/G2G3.e2.v0.html. We can see that the properties of the GMCs right before the second passage still resemble those of normal spiral galaxies, while GMCs after the second passage lie above the PHANGS trend in the σ_v vs Σ_{mol} plot and show significantly higher α_{vir} .

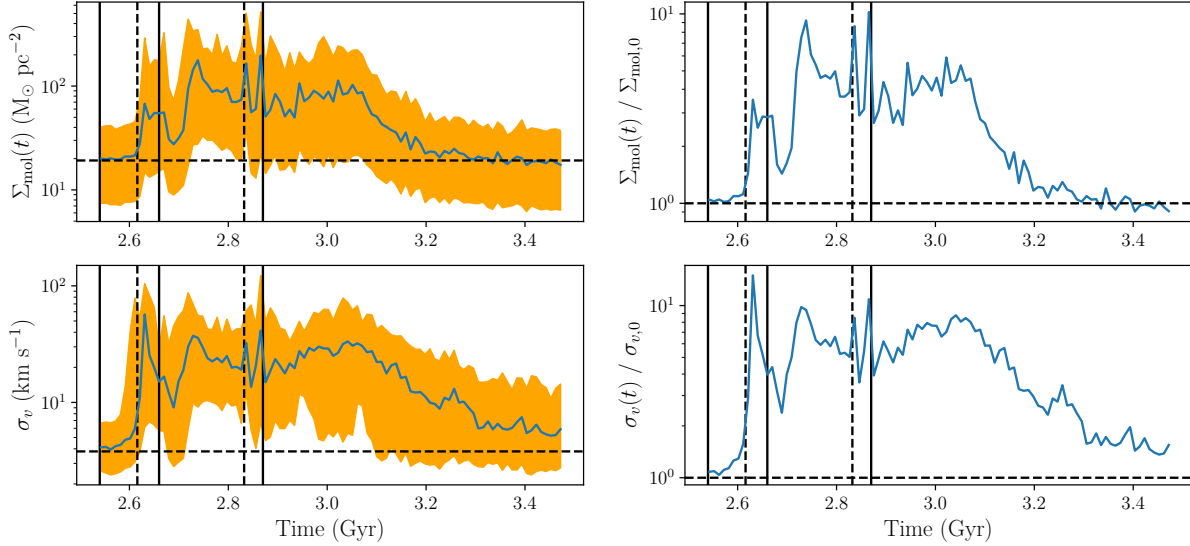


Figure 3. The Σ_{mol} and σ_v variation across the second passage and final coalescence of the G2&G3 merger at ‘e2’ orbit with viewing angle of ‘v0’. The two dashed vertical lines indicate the times when the simulated merger begin the second passage and experience final coalescence. The three solid vertical lines correspond to the 3 snapshots shown in Fig. 2. The horizontal dashed lines indicate the median value of the isolated G3 galaxy at time of 0.625 Gyr (Fig. 1) as a baseline for comparison. (*Upper left*) Σ_{mol} vs time. Blue lines shows the mass weighted median Σ_{mol} of the entire merger while the orange filled area indicates Σ_{mol} range between 16th and 84th percentile. The two dashed lines indicate the time for the start of the second passage and the final coalescence of the two nuclei. (*Upper right*) The ratio between median Σ_{mol} at given time and the median value $\Sigma_{\text{mol},0}$ for the isolated G3 galaxy at 0.625 Gyr. (*Lower left*) The mass-weighted median σ_v versus time. (*Lower right*) The ratio between the median σ_v and the value $\sigma_{v,0}$ for isolated G3 galaxies at 0.625 Gyr. We can see both Σ_{mol} and σ_v increase dramatically during the second passage when the extreme starburst happens.

values of the isolated G3 galaxy at 0.625 Gyr (Fig. 1) to show how the merging event affects the GMC properties during the second passage. Both Σ_{mol} and σ_v increase significantly during the merger, with a maximum increase of a factor of 10. The increase in σ_v and Σ_{mol} is roughly of the same order. Eq. 3 shows that a constant α_{vir} requires $\sigma_v^2 \propto \Sigma_{\text{mol}}$. These results imply that our simulated merger will have higher α_{vir} compared to PHANGS galaxies.

4.2. The virial parameters of GMCs

During the second passage, we see that the σ_v vs Σ_{mol} distribution for our simulated merger lies above the trend observed for the PHANGS galaxies. A higher σ_v for a given Σ_{mol} means the GMCs in these mergers are more turbulent and less gravitationally bound than in normal spiral galaxies.

We adopt the same approach as in observations to calculate α_{vir} for pixel-based GMC pixels using Eq. 3. Since the simulation data do not have a telescope “beam” and each pixel in this analysis is treated as an independent GMC, we set R to be half the size of each pixel (50 pc). With constant R , α_{vir} depends only on σ_v and Σ_{mol} . Higher σ_v at a similar Σ_{mol} thus implies that α_{vir} values for GMCs in simulated mergers

are higher than the values for PHANGS or simulated isolated galaxies. Higher values for α_{vir} are also found for NGC 3256 (Brunetti et al. 2020; Brunetti & Wilson 2022) and the Antennae (Brunetti 2022).

Fig. 4 shows α_{vir} as a function of time during the period near the second pericentric passage for the merger simulations with “e2” and “e1” orbits and viewed from “v0” angle. α_{vir} stays low before the second passage and suddenly rises after the passage along with a sudden increase in SFR. The peak of median α_{vir} can reach ~ 100 . After the second passage, α_{vir} gradually dies down as the SFR also decreases. During the entire merging process, we generally see a good correspondence between the SFR and α_{vir} peaks, which suggests that the α_{vir} value is either regulated by feedback from star formation or that both SFR and α_{vir} increase together as a result of the merger.

α_{vir} for our fiducial ‘e2’ orbit is generally higher than that of the ‘e1’ orbit and stays at higher values for a significantly longer time. The ‘e2’ orbit has a higher impact parameter than the ‘e1’ orbit (Section 2.1.2). Therefore, we would expect more gravitational potential energy transferred to the kinetic energy of individual GMCs, potentially making these GMCs less gravitationally bound. The α_{vir} values for the ‘e1’ orbit are more

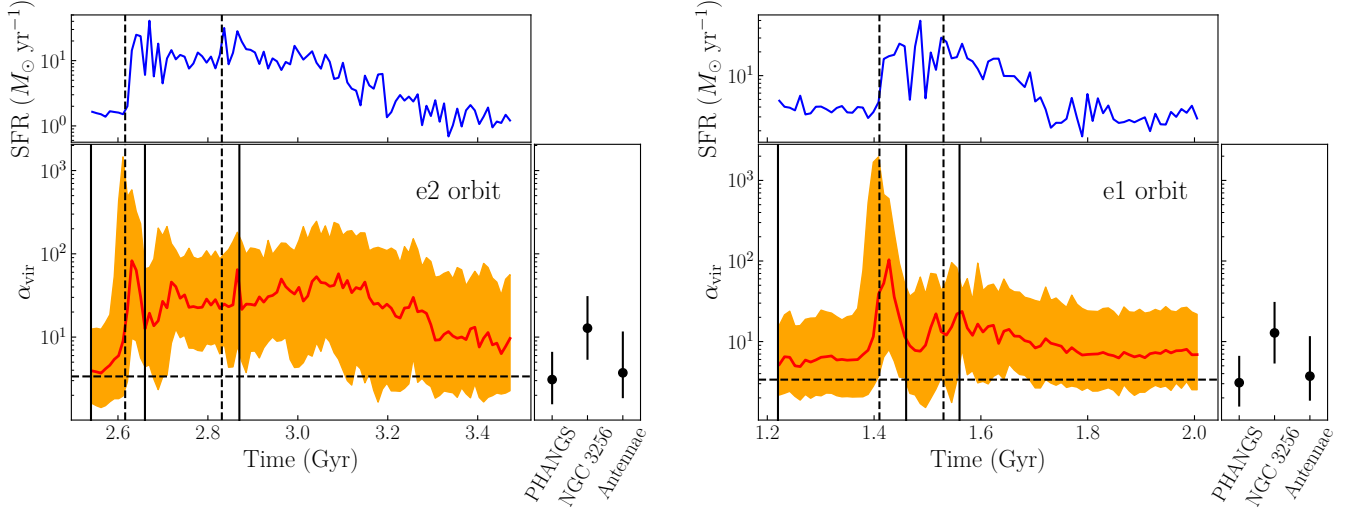


Figure 4. α_{vir} versus time for the G2&G3 mergers in (left) the e2 orbit and (right) the e1 orbit viewed from ‘v0’ angle during the final coalescence. (*Left*) The red line is the mass-weighted median for α_{vir} from the simulation. The orange shaded region includes data within the 16th and 84th quantile of α_{vir} values. The dashed lines correspond to the start of the second passage and the final coalescence of the two nuclei. The three solid lines correspond to the merger times shown in Fig. 2. The horizontal dashed line indicates the median α_{vir} for the isolated G3 galaxy at 0.625 Gyr (Fig. 1) as a baseline for comparison. The upper panel shows SFR versus time for the second coalescence and the right panel shows the 16th, 50th and 84th quantile of α_{vir} for PHANGS, NGC 3256 and the Antennae from the observations. In calculating α_{vir} , we use the U/LIRG α_{CO} for NGC 3256 and the Milky Way value for PHANGS and the Antennae. (*Right*) Same plot for G2&G3 merger in the ‘e1’ orbit during the final coalescence. The 3 solid lines correspond to 3 snapshots in Fig. C1. The ‘e1’ orbit has a smaller impact parameter than the ‘e2’ orbit. We can see the global α_{vir} increases dramatically right after the second passage as SFR rises. The peak SFR also roughly corresponds with the peak α_{vir} , which suggests the high α_{vir} might be caused by the feedback from the starburst.

similar to the α_{vir} of NGC 3256 and the Antennae and the ‘e1’ orbit is more similar to the orbit of the Antennae. We note that both the Antennae and NGC 3256 are at the very start of their second passages (Privon et al. 2013; Renaud et al. 2019a). At this stage, there are significant variations in α_{vir} , which makes it difficult to pick the exact snapshot that matches the observation. If we use the U/LIRG α_{CO} instead of the Milky Way value, α_{vir} for the Antennae would be similar to that of NGC 3256. We will discuss our α_{CO} choices further in Section 5.2.

4.3. Molecular Gas in the central 1 kpc region

From the moment 0 maps in Fig. 2, we can see that most molecular gas is concentrated in the center during the post-merger phase after 2.83 Gyr. This is consistent with the traditional scenario that the central starburst activity is caused by the inflow of molecular gas due to the loss of angular momentum (Hernquist 1989; Barnes & Hernquist 1991; Mihos & Hernquist 1994, 1996; Barnes & Hernquist 1996; Moreno et al. 2015). To quantify how much of the molecular gas is concentrated in the center, Fig. 5 shows the molecular gas mass within the central 1 kpc, and the ratio between this value and total molecular gas mass. The fraction of molecular

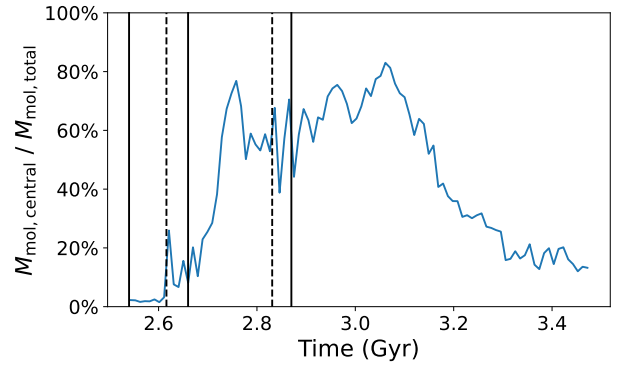


Figure 5. The ratio between molecular gas mass within the central 1 kpc radius circle of the G3 galaxy and total molecular gas inside our FOV of 25 kpc. During the second coalescence between 2.7 Gyr and 3.2 Gyr, more than 50% of molecular gas is concentrated within the central 1 kpc region, which indicates the Σ_{mol} increase we see in the simulated merger during the second passage is probably due to this gas concentration.

gas concentrated in the center reaches as high as 80% for a significant period of time (~ 500 Myr) around the final coalescence. On the other hand, Moreno et al. (2019) shows that the total molecular gas mass decreases during the second passage. Therefore, the overall high Σ_{mol}

values of GMCs across our simulated merger compared to isolated galaxies are mostly due to the central gas concentration.

Fig. 6 shows the σ_v versus Σ_{mol} distribution for pixels in the central kpc region of the G2&G3 merger at 2.87 Gyr (red aperture in Fig. 2), along with pixels in the center of PHANGS galaxies, the Antennae and NGC 3256. We can see the pixels in the center of the G2&G3 merger have a larger deviation from the PHANGS trend than NGC 3256, which indicates that the G2&G3 merger has GMCs with larger α_{vir} in the center. We also show the mass weighted median α_{vir} for the entire and central region of G2&G3 merger as a function of time (Fig. 6 right). α_{vir} in the center is generally higher than for the entire region, which indicates that GMCs in the center are more perturbed and less gravitationally bound. At the time right after the second passage, we see dramatic fluctuations of α_{vir} for both the center and the entire galaxy, which is probably due to the complex and constantly varying gas morphology during this period. Moreover, we might see two GMCs that are far apart in 3D space but lie along the same line of sight, which cause large measured α_{vir} value, but in a short time they no longer lie along the same line of sight, which causes a sudden drop of α_{vir} . At the post-merger phase, α_{vir} values are more stable. However, we see that α_{vir} of the disk region gradually settles down while the central α_{vir} keeps increasing. This might indicate that GMCs in the central region take more time to settle down to their normal states, which may be due to the starburst activity in the center. We also see high α_{vir} for the center at the very start (2.54 Gyr), which probably means GMCs in the center at this time have not recovered from the starburst event that occurred during the first peri-galactic passage.

4.4. Correlation between the central SFR and GMC Properties

The driving mechanism behind the SFR enhancement in mergers is of great interest to the study of star formation and galaxy evolution. One approach to tackle this problem is to decompose the SFR into the following 2 terms

$$\text{SFR} = \frac{M_{\text{mol}}}{t_{\text{dep}}}, \quad (4)$$

where t_{dep} is the depletion time, defined as the time for star formation to consume the available molecular gas. This approach makes it clearer that the rise in SFR could be either due to a larger amount of molecular gas “fuel driven”) or shorter depletion time (“efficiency driven”). The simulations (e.g. Moreno et al. 2021) and observations (e.g. Thorp et al. 2022) indicate that both

terms contribute to the SFR enhancement at kpc scales. Moreover, many studies of the Kennicutt-Schmidt relation in U/LIRGs at kpc scales show that these starburst mergers have relatively short t_{dep} of $\sim 10^8$ yr compared to normal spiral galaxies of $\sim 10^9$ yr (e.g. Daddi et al. 2010), which confirms the role of efficiency driving in mergers. With our simulations being able to probe the molecular gas at GMC scales, we can explore how t_{dep} is correlated with GMC populations in different regions.

For this analysis, we focus on the molecular gas and star formation in the central 1 kpc region since most gas is concentrated here during the second passage (see Section 4.3). We measure the mass-weighted median α_{vir} in this central region as a metric for GMC dynamical state in the center. Fig. 7 shows Σ_{mol} and Σ_{SFR} color-coded by α_{vir} for the central region as a function of time. We calculate the average Σ_{mol} and Σ_{SFR} by dividing the total M_{mol} or SFR in the central region by the aperture size. We show the data points within the period of 2.54 – 2.61 Gyr (before the second passage) and 2.73 – 3.47 Gyr (after the second passage) for comparison. We exclude the data points between the start of the second passage (2.62 Gyr) and the time when the central/total gas fraction starts to reach 50% (2.73 Gyr) because data points from this period show a large deviation from the major trend in Σ_{SFR} vs Σ_{mol} diagram. The large deviation is probably because the limited amount of molecular gas is highly perturbed in the central region. Gas is either quickly consumed without being replenished in time, or just concentrated and has not formed stars yet, which causes the large scatter in the Σ_{SFR} vs Σ_{mol} relation. On the other hand, before and after this period, the central region is in a relatively stable state when the molecular gas is constantly replenished to fuel star formation activity.

In the left panel of Fig. 7, we can see that t_{dep} becomes shorter as Σ_{mol} and Σ_{SFR} increase. The points at the lower left end of the Σ_{mol} correspond to the times before the second passage, which also have relatively low α_{vir} . In contrast, the α_{vir} after the second passage is significantly higher. We also note that t_{dep} even before the second passage ($\sim 10^8$ yr) is quite shorter than that of normal spiral galaxies (10^9 yr). The difference could be due to different dynamical timescales of simulated and observed galaxies. At this time, we can see α_{vir} for the central region is already ~ 10 which indicates the molecular gas in the central region has already been disturbed.

There is no significant correlation between t_{dep} and α_{vir} , with Spearman coefficient of -0.08 for all data points and of 0.18 for data after the second passage, which is against our expectation that low α_{vir} gas form

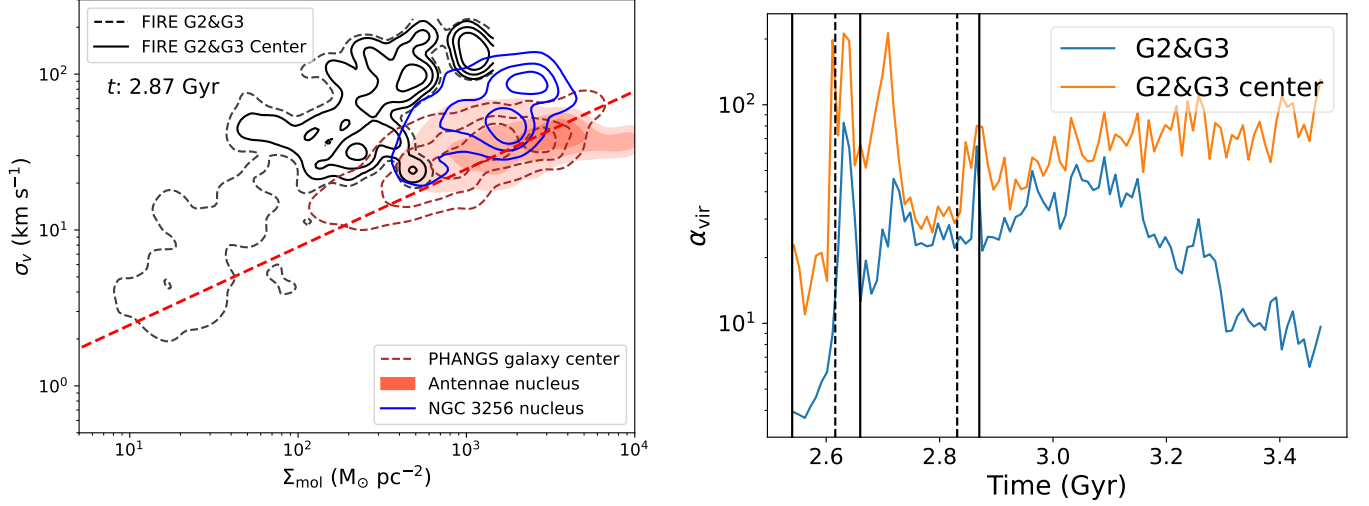


Figure 6. (*Left*) The σ_v versus Σ_{mol} contour for the entire (dashed contour) and central 1 kpc region (solid contour) of the G2&G3 merger at 2.87 Gyr viewed from the ‘v0’ angle. We also show contours for the centers of PHANGS galaxies (brown dashed contours), the Antennae (orange shaded contours) and NGC 3256 (blue contours). We can see the central region in our simulated merger generally has the highest σ_v and α_{vir} . (*Right*) The mass weighted median α_{vir} for molecular gas in the entire (blue) and central (orange) region of G2&G3 merger viewed from ‘v0’ angle. We see that α_{vir} for the entire disk gradually settles back to the original low value, while that for the central region keeps a high value until the end of the simulation.

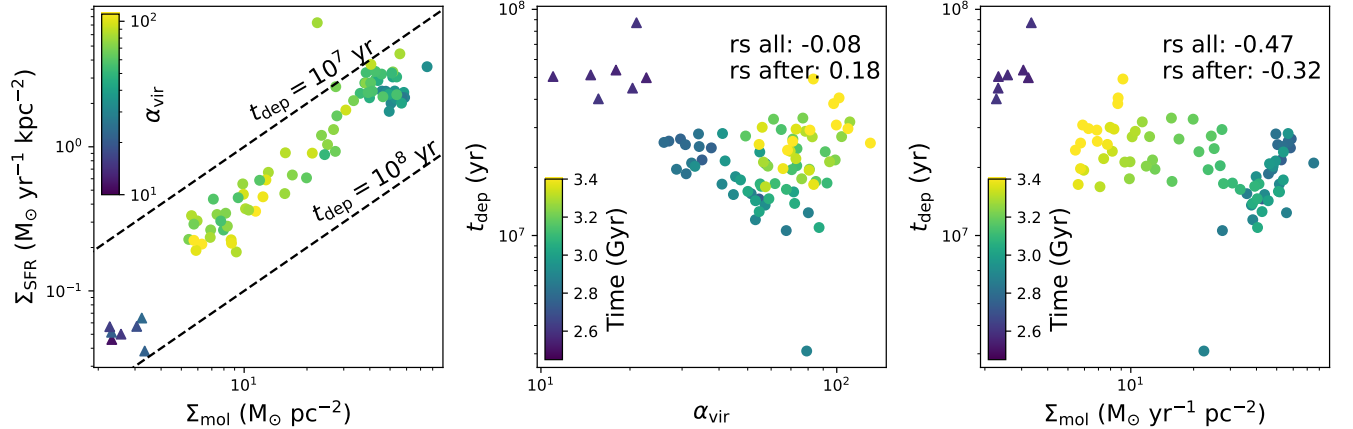


Figure 7. (*Left*) SFR surface density Σ_{SFR} versus Σ_{mol} color coded by the mass-weighted median α_{vir} for the central 1 kpc region of the the G2&G3 merger during the second passage of the ‘e2’ orbit viewed from ‘v0’ orientation. We include simulated data points within 2.54 – 2.61 Gyr (before the second passage; triangle) and 2.73 – 3.47 Gyr (after the second passage; circle). Both Σ_{SFR} and Σ_{mol} are calculated as total central SFR or M_{mol} within 1 kpc radius divided by the aperture size, while α_{vir} is the mass weighted median of pixels inside the aperture. The two dashed line indicate constant depletion times ($t_{\text{dep}} = \Sigma_{\text{mol}}/\Sigma_{\text{SFR}}$) of 10^7 and 10^8 years. (*Middle*) t_{dep} versus α_{vir} for the central 1 kpc. (*Right*) t_{dep} versus Σ_{mol} for the central region. The label “rs all” shows the Spearman coefficient between t_{dep} and α_{vir} and Σ_{mol} for all data points while “rs after” shows the Spearman coefficient only for data after the second passage. We can see there is no significant correlation between α_{vir} and t_{dep} , which is against our expectation that low α_{vir} clouds will consume molecular gas at faster rate.

stars more quickly. We can also clearly see a distinction between α_{vir} before and after the second passage. The α_{vir} before the second passage is relatively small and corresponds to larger t_{dep} while the α_{vir} after the second passage is significantly larger but corresponds to shorter t_{dep} . This again is inconsistent with our expectation that low α_{vir} GMCs should form stars more easily.

Other physical mechanisms rather than self-gravity of individual GMCs may be needed to help the molecular gas to collapse (see detailed discussion in Section 5.1).

On the other hand, we see an anti-correlation between t_{dep} and Σ_{mol} . This relation is similar to the global Kennicutt-Schmidt relation where the gas rich U/LIRGs have the shorter t_{dep} (Daddi et al. 2010). One expla-

nation for this trend is that the fraction of dense gas (traced by HCN) that are actually forming stars (i.e. traces the self-gravitating gas fraction) is increasing as Σ_{mol} increases (e.g. Gao & Solomon 2004; Bemis & Wilson 2023). If we assume Σ_{mol} is proportional to the mean volume density of molecular gas in the central region, we would expect larger fraction of molecular gas above the dense gas threshold ($n > 10^4 \text{ cm}^{-3}$) in FIRE-2 simulation (Hopkins 2015), which leads to faster star formation and shorter t_{dep} .

5. DISCUSSION

5.1. How can high α_{vir} gas form stars in simulated mergers?

As shown in Section 4.2, α_{vir} generally stays above 10 during the second passage for the G2&G3 merger. If we assume star formation occurs in individual GMCs and is driven by the collapse of the clouds due to self-gravity, we would expect star forming GMCs to have α_{vir} below 1. The combination of high α_{vir} values and starburst activity is inconsistent with this expectation, unless the velocity dispersion is being driven to higher values by infall motion. Furthermore, we find no correlation between α_{vir} and t_{dep} (Section 4.4), which suggests low α_{vir} values do not strongly affect the depletion time in our simulations. However, we need to note that our measurement of α_{vir} from pixel-based method might not reflect the real α_{vir} of individual GMC components, especially for the post-second-passage phase when molecular gas is concentrated in the center. Although observations (Brunetti & Wilson 2022; Sun et al. 2020) show that cloud properties extracted from a pixel-based approach is generally consistent with the traditional cloud-based approach, they also show the pixel-based approach gives higher σ_v and α_{vir} for molecular gas in galaxy centers. This is likely due to the superimposition of different GMC components along the same line of sight in gas-concentrated galaxy centers. Sun et al. (2022) find that α_{vir} from pixel-based approach is ~ 3 times higher than the cloud-based approach for galaxy centers. If we assume the same degree of overestimate in our simulation data for the merger center, we would expect the real α_{vir} to be ~ 10 during the second passage, still significantly higher than the critical value of 1 when clouds reach the self-collapsing criterion. We also note that even the observational cloud-based approach by extracting different GMC components from p-p-v data cube might still suffer from the projection effects. Beaumont et al. (2013) find that α_{vir} from p-p-p and p-p-v cubes have a factor of 2 difference for substructures in their cloud simulation due to a mismatch of substructures from these two data cubes. Therefore, one of our next steps is to perform

cloud-finding algorithm (Burkhart et al. 2013) on both p-p-p and p-p-v simulation data cubes to fully understand how GMCs evolve during the merging events.

A possible explanation for large α_{vir} is that GMCs that satisfy the self-collapsing criterion have already formed stars and become unbound or destroyed due to the stellar feedback. However, if this is the case, we would expect α_{vir} to fluctuate around the critical value of 1. Furthermore, according to Benincasa et al. (2020), GMCs with high α_{vir} (>10) have significantly shorter lifetimes (~ 2 Myr) than GMCs with low α_{vir} (~ 1 ; lifetime of ~ 10 Myr). If we assume all GMCs are of the same population but at different evolutionary stages, we would expect GMCs to stay at low α_{vir} state for a longer time and hence we should be more likely to catch these low α_{vir} GMCs in our simulation snapshots. Instead, we see α_{vir} constantly higher than 10 during the starburst activity (Fig. 4), which is inconsistent with this scenario.

It is perhaps likely that the explanation is that these GMCs are experiencing compression from the large-scale gravitational potential. This compression could add additional potential energy to balance the kinetic energy. Furthermore, they can trigger inflow of gas into GMCs and bring radial velocity (V_r) component into our σ_v measurement. Ganguly et al. (2022) find in their simulation that v_r could be an important factor to produce high measured α_{vir} clouds. For GMCs in normal spiral galaxies and galaxy pairs (e.g., M 51), Meidt et al. (2018) show that the large-scale stellar potential could be responsible for holding individual GMCs in energy equipartition state. Compared to galaxies in their study, the starburst mergers in our study undergo more dramatic morphological changes, which could generate complicated gravitational tidal fields. Renaud et al. (2009) show in their simulation that major mergers can produce fully compressive tidal fields that concentrate molecular gas and trigger starburst activities. These compressive tidal fields are believed to be responsible for creating the off-nuclei gas concentration region in the ULIRG, Arp 220 (Downes & Solomon 1998). In our next step to test this scenario, we will need to calculate tidal deformation timescale (as in Ganguly et al. 2022) for each individual GMC and compare it with GMC free-fall and crossing timescales to see how important the external tidal field is compared to GMC self-gravity.

Another possible explanation is that molecular gas is smoothly distributed rather than clumped into individual GMCs during the starburst activities. If this is the case, the star formation is regulated by the entire molecular disk rather than individual GMC components (Krumholz et al. 2018). Wilson et al. (2019) pro-

pose that the star formation in U/LIRGs is regulated by the hydrodynamic pressure of the molecular disk with a constant scale height. In observation, one way to test the smoothness of gas distribution is by comparing average gas surface density at different observing resolutions (Leroy et al. 2017). Brunetti et al. (2020) show that molecular gas in the LIRG, NGC 3256, is smoothly distributed based on this method. For our simulated merger, gas might be smoothly distributed during the second passage when most gas is concentrated in the center (e.g. at 2.87 Gyr, Fig. 2). We could test this scenario by changing the pixel size in our p-p-v cubes and compare the average gas surface densities in the central region at different pixel resolutions.

5.2. Comparison with observations

As shown in Section 4, our simulated merger generally has lower Σ_{mol} and higher σ_v and α_{vir} compared to the two observed mergers, the Antennae and NGC 3256. We note that this simulation is not set to match the exact condition of the observed mergers, so some discrepancy between observations and simulations would be expected. From the observational side, the biggest uncertainty that comes into the measurement is the value of α_{CO} . As mentioned in Section 4.1, if we adopt the ULIRG α_{CO} instead of the Milky Way value for the Antennae, we would find the Antennae to have similar Σ_{mol} and α_{vir} as NGC 3256. In contrast, if we assume an even smaller α_{CO} for NGC 3256, that might bring the contours of the observations further away from the PHANGS trend and hence more similar to the simulation contours. However, various LVG modelings (Papadopoulos et al. 2012; Harrington et al. 2021) show that local U/LIRGs and high- z starburst galaxies generally have α_{CO} above $0.8 \text{ M}_{\odot} (\text{K km s}^{-1} \text{ pc}^2)^{-1}$. In fact, a recent study by Dunne et al. (2022) concludes that these starburst galaxies might actually have α_{CO} equal to the Milky Way value by cross-correlating the CO luminosity with dust and CI luminosity. Therefore, a factor of 3 discrepancy in α_{vir} between simulated mergers and NGC 3256 is probably real rather than due to measurement uncertainties.

For the comparison between observations and simulations, we also note that the two observed mergers are both in an early stage after the second passage since we can still identify two separate nuclei. In this stage, α_{vir} is quite time-sensitive and it is difficult to match the exact same stage between the simulated and observed galaxies. Therefore, it is possible that both NGC 3256 and Antennae are caught at a specific merger stage with a lower α_{vir} (although in the case of NGC 3256, still enhanced relative to PHANGS galaxies). In compari-

son, α_{vir} in the simulations is relatively stable in the post-merger stage. This stability suggests that a comparison between simulations and observations of post-merger galaxies could be a useful next step. Moreover, post-mergers have a rather simple morphology, which simplifies the task of making quantitative comparisons.

It would also be interesting to compare the simulation results with starburst galaxies at high redshift. Recent works (e.g. Dessauges-Zavadsky et al. 2019; Meštrić et al. 2022) show that we can probe GMC-scale star-forming clumps in gravitationally lensed objects at high redshift. These star-forming clumps generally show a similar α_{vir} to GMCs of normal spiral galaxies in our local Universe despite using different α_{CO} , and therefore lower than what we see in the simulations. However, these high- z targets likely live in a completely different environment than our idealized mergers. Specifically, high- z galaxies tend to have a much higher gas fraction, and thus can form self-gravitating clumps with low α_{vir} more easily (Fensch & Bournaud 2021).

5.3. Comparison with other simulations

In this work, we use the non-cosmological simulations from Moreno et al. (2019) to compare GMC properties in mergers and normal spiral galaxies. Two major advantages of this simulation suite are that it has a resolution of 1.1 pc (which is much smaller than typical GMC sizes) and it can model the ISM down to low temperatures (~ 10 K), both of which allow us to match the molecular gas in simulations with CO observations. Various cosmological simulations show that mergers are responsible for enhancing gas fractions and triggering starburst activity (Scudder et al. 2015; Knapen et al. 2015; Patton et al. 2013; Martin et al. 2017; Rodríguez Montero et al. 2019; Patton et al. 2020, e.g.). However, these simulations can only model gas with temperatures down to 10^4 K and hence are incapable of capturing the turbulent multi-phase structure of the ISM. An alternative approach is to compare observations with cosmological zoom-in simulations, which allows for higher resolution, more realistic feedback star formation thresholds, and more realistic modeling of the multi-phase ISM. Various authors have explored GMC properties, mostly in Milky-Way-like galaxies (e.g. Guedes et al. 2011; Ceverino et al. 2014; Sawala et al. 2014; Benincasa et al. 2020; Orr et al. 2021), and they generally reproduce the GMC mass function in our Milky Way. However, only a handful of work (e.g. Rey et al. 2022) has been done for GMCs in mergers. Also, the Milky Way is identified as a green-valley galaxy (Mutch et al. 2011) with lower SFR than typical spiral galaxies in the local universe. Therefore, due to the lack of zoom-in cosmological simulations

on local mergers, we have adopted idealized simulations for this study. Furthermore, idealized simulations allow us to compare GMCs of control galaxies with those of mergers to directly study the impact of the merging event.

Several idealized simulations have been performed to study molecular gas and GMC properties in mergers. [Karl et al. \(2013\)](#) perform a merger simulation closely matched to the Antennae and find a great match on CO distributions between simulation and observations, which suggests insufficient stellar feedback efficiencies in the Antennae. [Li et al. \(2022\)](#) perform a study of GMCs and young massive star clusters (YMCs) in Antennae-like mergers. They find that GMC mass functions for mergers have similar power-law slopes to normal spirals during the second coalescence but with much higher mass values. [Narayanan et al. \(2011\)](#) compare the α_{CO} in mergers and normal spiral galaxies and find that the low α_{CO} in mergers is mostly due to the high temperature and α_{vir} of GMCs in the merger. They predict there is a transition stage with α_{CO} between U/LIRG and Milky Way values and that α_{vir} is tightly anti-correlated with α_{CO} . In contrast, [Renaud et al. \(2019b\)](#) show that α_{CO} values drop quickly during each coalescence between two galaxies. We find similar behavior for α_{vir} during the second coalescence, which might imply a similar drop in α_{CO} ([Narayanan et al. 2011](#)).

6. CONCLUSIONS

We summarize our main conclusions below:

- Our pixel-by-pixel analysis shows that the FIRE-2 simulation by [Moreno et al. \(2019\)](#) successfully reproduces the σ_v vs Σ_{mol} relation for GMC-scale pixels measured for galaxies in the PHANGS survey.
- The simulated mergers show a significant increase in both Σ_{mol} and σ_v for GMC-pixels by a factor of 5 – 10 during the second passage when SFR peaks, which brings these pixels above PHANGS-trend in the σ_v vs Σ_{mol} diagram. This may indicate GMCs in these mergers are less gravitationally bound. We quantify this deviation by the virial parameter α_{vir} and find that our simulated mergers have α_{vir} of 10 – 100, which is even higher than the observed α_{vir} in NGC 3256. However, this discrepancy could be partly due to the high impact parameter in the initial set-up of the simulated mergers. Furthermore, we see a good correspondence between the increase in SFR and α_{vir} , which suggest either the starburst feedback is responsi-

ble for dispersing the gas or the correlation is in response to gas compression.

- Our simulated mergers show a clear gas concentration in the center during the second passage, with up to 80% of molecular gas in the central 1 kpc region. Therefore, the GMC-pixels in the central region tend to have the highest Σ_{mol} . We also find these pixels tend to have the highest σ_v and α_{vir} , which could be caused by the starburst feedback and the inflow of gas.
- We explore if α_{vir} at GMC scales is responsible for the varying depletion time (t_{dep}) in observed mergers. While we do not find a significant correlation between t_{dep} and α_{vir} , we see a clear distinction before (small α_{vir} , long t_{dep}) and after (large α_{vir} , short t_{dep}) the second passage. This could be due to projection effects (multiple GMCs along the same line of sight) during the second passage when most of the molecular gas is concentrated in the central 1 kpc region. The next step is to run a cloud-identification algorithm on the data to disentangle this factor. We also suspect there might be some other mechanism, such as the stellar potential and inflow of gas, that helps the GMCs in starburst mergers to collapse and form stars. We also find that t_{dep} has a significant anti-correlation with Σ_{mol} for the central region. This may be due to higher Σ_{mol} leading to a higher fraction of dense gas, which shortens t_{dep} .

In the future, we would like to expand our comparison to more observed and simulated mergers. From the observational side, we need larger samples of galaxy mergers spanning different evolutionary stages in order to understand how GMCs evolve throughout the merging. In addition, it is easier to compare the observations with simulations in the post-merger stage since the morphology is simpler and easier to quantify. The ALMA archive contains ~ 40 U/LIRGs with GMC resolution CO 2-1 observations that can be used to build a more complete sample of GMCs in mergers at different stages. From the simulation side, it would be helpful to have simulations that better match the observed galaxies. The Antennae has been widely studied and matched by non-cosmological simulations (e.g. [Renaud et al. 2019a](#); [Li et al. 2022](#)) but NGC 3256 is less well studied. Besides comparing with these non-cosmological simulations, we could also compare observation with cosmological simulations, such as FIREBox ([Feldmann et al. 2022](#)), that include local mergers.

We thank Dr. Jiayi Sun for his help to access to PHANGS data and insightful discussions about the comparison between simulation and observation. We thank Dr. Nathan Brunetti for access to CO 2-1 image and GMC catalogs of the observed mergers in his paper.

This work was carried out as part of the FIRE collaboration. The research of C.D.W. is supported by grants from the Natural Sciences and Engineering Research Council of Canada and the Canada Research Chairs program. The research of H.H. is partially supported by the New Technologies for Canadian Observatories, an NSERC-CREATE training program. The computations in this paper were run on the Odyssey cluster supported by the FAS Division of Science, Research Computing Group at Harvard University. Support for JM is provided by the Hirsch Foundation, by the NSF (AST Award Number 1516374), and by the Harvard Institute for Theory and Computation, through their Visiting Scholars Program. B.B. acknowledges support from NSF grant AST-2009679. B.B. is grateful for the gener-

ous support of the David and Lucile Packard Foundation and Alfred P. Sloan Foundation. The Flatiron Institute is supported by the Simons Foundation.

This paper makes use of the following ALMA data: ADS/JAO.ALMA #2015.1.00714.S and ADS/JAO.ALMA #2018.1.00272.S. ALMA is a partnership of ESO (representing its member states), NSF (USA), and NINS (Japan), together with NRC (Canada), MOST and ASIAA (Taiwan), and KASI (Republic of Korea), in cooperation with the Republic of Chile. The Joint ALMA Observatory is operated by ESO, AUI/ NRAO, and NAOJ. The National Radio Astronomy Observatory is a facility of the National Science Foundation operated under cooperative agreement by Associated Universities, Inc.

Facilities: ALMA

Software: astropy (Collaboration et al. 2013), Spectral-Cube (Ginsburg et al. 2019)

REFERENCES

- Barnes, J. E., & Hernquist, L. 1996, *The Astrophysical Journal*, 471, 115, doi: [10.1086/177957](https://doi.org/10.1086/177957)
- Barnes, J. E., & Hernquist, L. E. 1991, *The Astrophysical Journal*, 370, L65, doi: [10.1086/185978](https://doi.org/10.1086/185978)
- Beaumont, C. N., Offner, S. S. R., Shetty, R., Glover, S. C. O., & Goodman, A. A. 2013, *The Astrophysical Journal*, 777, 173, doi: [10.1088/0004-637X/777/2/173](https://doi.org/10.1088/0004-637X/777/2/173)
- Bellochi, E., Pereira-Santaella, M., Colina, L., et al. 2022, *A&A*, 664, A60, doi: [10.1051/0004-6361/202142802](https://doi.org/10.1051/0004-6361/202142802)
- Bemis, A. R., & Wilson, C. D. 2023, arXiv e-prints, arXiv:2301.06478. <https://arxiv.org/abs/2301.06478>
- Benincasa, S. M., Loebman, S. R., Wetzel, A., et al. 2020, *Monthly Notices of the Royal Astronomical Society*, 497, 3993, doi: [10.1093/mnras/staa2116](https://doi.org/10.1093/mnras/staa2116)
- Bolatto, A. D., Leroy, A. K., Rosolowsky, E., Walter, F., & Blitz, L. 2008, *The Astrophysical Journal*, 686, 948, doi: [10.1086/591513](https://doi.org/10.1086/591513)
- Bottrell, C., & Hani, M. H. 2022, *Monthly Notices of the Royal Astronomical Society*, 514, 2821, doi: [10.1093/mnras/stac1532](https://doi.org/10.1093/mnras/stac1532)
- Bottrell, C., Hani, M. H., Teimoorinia, H., Patton, D. R., & Ellison, S. L. 2022, *Monthly Notices of the Royal Astronomical Society*, 511, 100, doi: [10.1093/mnras/stab3717](https://doi.org/10.1093/mnras/stab3717)
- Bottrell, C., Hani, M. H., Teimoorinia, H., et al. 2019, *Monthly Notices of the Royal Astronomical Society*, 490, 5390, doi: [10.1093/mnras/stz2934](https://doi.org/10.1093/mnras/stz2934)
- Bournaud, F., Duc, P. A., & Emsellem, E. 2008, *Monthly Notices of the Royal Astronomical Society*, 389, L8, doi: [10.1111/j.1745-3933.2008.00511.x](https://doi.org/10.1111/j.1745-3933.2008.00511.x)
- Brunetti, N. 2022, Thesis
- Brunetti, N., & Wilson, C. D. 2022, *Monthly Notices of the Royal Astronomical Society*, 515, 2928, doi: [10.1093/mnras/stac1975](https://doi.org/10.1093/mnras/stac1975)
- Brunetti, N., Wilson, C. D., Sliwa, K., et al. 2020, *Monthly Notices of the Royal Astronomical Society*, 500, 4730, doi: [10.1093/mnras/staa3425](https://doi.org/10.1093/mnras/staa3425)
- Burkhart, B. 2018, *ApJ*, 863, 118, doi: [10.3847/1538-4357/aad002](https://doi.org/10.3847/1538-4357/aad002)
- Burkhart, B., Collins, D. C., & Lazarian, A. 2015, *The Astrophysical Journal*, 808, 48, doi: [10.1088/0004-637X/808/1/48](https://doi.org/10.1088/0004-637X/808/1/48)
- Burkhart, B., Lazarian, A., Goodman, A., & Rosolowsky, E. 2013, *ApJ*, 770, 141, doi: [10.1088/0004-637X/770/2/141](https://doi.org/10.1088/0004-637X/770/2/141)
- Burkhart, B., & Mocz, P. 2019, *ApJ*, 879, 129, doi: [10.3847/1538-4357/ab25ed](https://doi.org/10.3847/1538-4357/ab25ed)
- Burkhart, B., Appel, S. M., Bialy, S., et al. 2020, *The Astrophysical Journal*, 905, 14, doi: [10.3847/1538-4357/abc484](https://doi.org/10.3847/1538-4357/abc484)
- Catinella, B., Saintonge, A., Janowiecki, S., et al. 2018, *Monthly Notices of the Royal Astronomical Society*, 476, 875, doi: [10.1093/mnras/sty089](https://doi.org/10.1093/mnras/sty089)

- Ceverino, D., Klypin, A., Klimek, E. S., et al. 2014, *Monthly Notices of the Royal Astronomical Society*, 442, 1545, doi: [10.1093/mnras/stu956](https://doi.org/10.1093/mnras/stu956)
- Chevance, M., Kruijssen, J. M. D., Hygate, A. P. S., et al. 2020, *Monthly Notices of the Royal Astronomical Society*, 493, 2872, doi: [10.1093/mnras/stz3525](https://doi.org/10.1093/mnras/stz3525)
- Collaboration, T. A., Robitaille, T. P., Tollerud, E. J., et al. 2013, *A&A*, 558, A33, doi: [10.1051/0004-6361/201322068](https://doi.org/10.1051/0004-6361/201322068)
- Colombo, D., Hughes, A., Schinnerer, E., et al. 2014, *The Astrophysical Journal*, 784, 3, doi: [10.1088/0004-637X/784/1/3](https://doi.org/10.1088/0004-637X/784/1/3)
- Colombo, D., Rosolowsky, E., Duarte-Cabral, A., et al. 2019, *Monthly Notices of the Royal Astronomical Society*, 483, 4291, doi: [10.1093/mnras/sty3283](https://doi.org/10.1093/mnras/sty3283)
- Daddi, E., Elbaz, D., Walter, F., et al. 2010, *The Astrophysical Journal*, 714, L118, doi: [10.1088/2041-8205/714/1/L118](https://doi.org/10.1088/2041-8205/714/1/L118)
- Dale, J. E., Ngoumou, J., Ercolano, B., & Bonnell, I. A. 2014, *Monthly Notices of the Royal Astronomical Society*, 442, 694, doi: [10.1093/mnras/stu816](https://doi.org/10.1093/mnras/stu816)
- Decataldo, D., Lupi, A., Ferrara, A., Pallottini, A., & Fumagalli, M. 2020, *Monthly Notices of the Royal Astronomical Society*, 497, 4718, doi: [10.1093/mnras/staa2326](https://doi.org/10.1093/mnras/staa2326)
- Dessauges-Zavadsky, M., Richard, J., Combes, F., et al. 2019, *Nat Astron*, 3, 1115, doi: [10.1038/s41550-019-0874-0](https://doi.org/10.1038/s41550-019-0874-0)
- Donovan Meyer, J., Koda, J., Momose, R., et al. 2013, *The Astrophysical Journal*, 772, 107, doi: [10.1088/0004-637X/772/2/107](https://doi.org/10.1088/0004-637X/772/2/107)
- Downes, D., & Solomon, P. M. 1998, *ApJ*, 507, 615, doi: [10.1086/306339](https://doi.org/10.1086/306339)
- Dunne, L., Maddox, S. J., Papadopoulos, P. P., Ivison, R. J., & Gomez, H. L. 2022, *Monthly Notices of the Royal Astronomical Society*, 517, 962, doi: [10.1093/mnras/stac2098](https://doi.org/10.1093/mnras/stac2098)
- Elmegreen, D. M., Elmegreen, B. G., Kaufman, M., et al. 2017, *The Astrophysical Journal*, 841, 43, doi: [10.3847/1538-4357/aa6ba5](https://doi.org/10.3847/1538-4357/aa6ba5)
- Fall, S. M., Krumholz, M. R., & Matzner, C. D. 2010, *Astrophysical Journal Letters*, 710, 142, doi: [10.1088/2041-8205/710/2/L142](https://doi.org/10.1088/2041-8205/710/2/L142)
- Feldmann, R., Quataert, E., Faucher-Giguère, C.-A., et al. 2022, *FIREbox: Simulating Galaxies at High Dynamic Range in a Cosmological Volume*
- Fensch, J., & Bournaud, F. 2021, *Monthly Notices of the Royal Astronomical Society*, 505, 3579, doi: [10.1093/mnras/stab1489](https://doi.org/10.1093/mnras/stab1489)
- Fensch, J., Renaud, F., Bournaud, F., et al. 2017, *Monthly Notices of the Royal Astronomical Society*, 465, 1934, doi: [10.1093/mnras/stw2920](https://doi.org/10.1093/mnras/stw2920)
- Fukui, Y., Kawamura, A., Minamidani, T., et al. 2008, *The Astrophysical Journal Supplement Series*, 178, 56, doi: [10.1086/589833](https://doi.org/10.1086/589833)
- Ganguly, S., Walch, S., Clarke, S. D., & Seifried, D. 2022, *SILCC-Zoom: The Dynamic Balance in Molecular Cloud Substructures*
- Gao, Y., & Solomon, P. M. 2004, *The Astrophysical Journal*, 606, 271, doi: [10.1086/382999](https://doi.org/10.1086/382999)
- Ginsburg, A., Koch, E., Robitaille, T., et al. 2019, *Zenodo*, doi: [10.5281/zenodo.2573901](https://doi.org/10.5281/zenodo.2573901)
- Grudić, M. Y., Hopkins, P. F., Faucher-Giguère, C. A., et al. 2018, *Monthly Notices of the Royal Astronomical Society*, 475, 3511, doi: [10.1093/MNRAS/STY035](https://doi.org/10.1093/MNRAS/STY035)
- Guedes, J., Callegari, S., Madau, P., & Mayer, L. 2011, *The Astrophysical Journal*, 742, 76, doi: [10.1088/0004-637X/742/2/76](https://doi.org/10.1088/0004-637X/742/2/76)
- Guszejnov, D., Hopkins, P. F., & Ma, X. 2017, *Monthly Notices of the Royal Astronomical Society*, 472, 2107, doi: [10.1093/mnras/stx2067](https://doi.org/10.1093/mnras/stx2067)
- Harrington, K. C., Weiss, A., Yun, M. S., et al. 2021, *The Astrophysical Journal*, 908, 95, doi: [10.3847/1538-4357/abcc01](https://doi.org/10.3847/1538-4357/abcc01)
- Hennebelle, P., & Chabrier, G. 2011, *The Astrophysical Journal*, 743, L29, doi: [10.1088/2041-8205/743/2/L29](https://doi.org/10.1088/2041-8205/743/2/L29)
- Hernquist, L. 1989, *Nature*, 340, 687, doi: [10.1038/340687a0](https://doi.org/10.1038/340687a0)
- Heyer, M., & Dame, T. M. 2015, *Annual Review of Astronomy and Astrophysics*, vol. 53, p.583-629, 53, 583, doi: [10.1146/annurev-astro-082214-122324](https://doi.org/10.1146/annurev-astro-082214-122324)
- Heyer, M., Krawczyk, C., Duval, J., & Jackson, J. M. 2009, *The Astrophysical Journal*, 699, 1092, doi: [10.1088/0004-637X/699/2/1092](https://doi.org/10.1088/0004-637X/699/2/1092)
- Hopkins, P. F. 2015, *Monthly Notices of the Royal Astronomical Society*, 450, 53, doi: [10.1093/mnras/stv195](https://doi.org/10.1093/mnras/stv195)
- . 2017, *A New Public Release of the GIZMO Code*
- Hopkins, P. F., Wetzel, A., Kereš, D., et al. 2018, *Monthly Notices of the Royal Astronomical Society*, 480, 800, doi: [10.1093/mnras/sty1690](https://doi.org/10.1093/mnras/sty1690)
- Howard, C. S., Pudritz, R. E., & Harris, W. E. 2018, *Nature Astronomy*, 2, 725, doi: [10.1038/s41550-018-0506-0](https://doi.org/10.1038/s41550-018-0506-0)
- Howell, J. H., Armus, L., Mazzarella, J. M., et al. 2010, *The Astrophysical Journal*, 715, 572, doi: [10.1088/0004-637X/715/1/572](https://doi.org/10.1088/0004-637X/715/1/572)
- Hughes, A., Meidt, S. E., Colombo, D., et al. 2013, *The Astrophysical Journal*, 779, 46, doi: [10.1088/0004-637X/779/1/46](https://doi.org/10.1088/0004-637X/779/1/46)

- Jeffreson, S. M. R., & Kruijssen, J. M. D. 2018, *Monthly Notices of the Royal Astronomical Society*, 28, 1, doi: [10.1093/mnras/sty594](https://doi.org/10.1093/mnras/sty594)
- Karl, S. J., Lunttila, T., Naab, T., et al. 2013, *Monthly Notices of the Royal Astronomical Society*, 434, 696, doi: [10.1093/mnras/stt1063](https://doi.org/10.1093/mnras/stt1063)
- Karl, S. J., Naab, T., Johansson, P. H., et al. 2010, *The Astrophysical Journal*, 715, L88, doi: [10.1088/2041-8205/715/2/L88](https://doi.org/10.1088/2041-8205/715/2/L88)
- Kennicutt, R. C., & Evans, N. J. 2012, *Annual Review of Astronomy and Astrophysics*, 50, 531, doi: [10.1146/annurev-astro-081811-125610](https://doi.org/10.1146/annurev-astro-081811-125610)
- Kennicutt, Jr., R. C. 1998, *The Astrophysical Journal*, 498, 541, doi: [10.1086/305588](https://doi.org/10.1086/305588)
- Kim, C.-G., Ostriker, E. C., & Raileanu, R. 2017, *The Astrophysical Journal*, 834, 25, doi: [10.3847/1538-4357/834/1/25](https://doi.org/10.3847/1538-4357/834/1/25)
- Knapen, J. H., Cisternas, M., & Querejeta, M. 2015, *Monthly Notices of the Royal Astronomical Society*, 454, 1742, doi: [10.1093/mnras/stv2135](https://doi.org/10.1093/mnras/stv2135)
- Krumholz, M. R., Burkhardt, B., Forbes, J. C., & Crocker, R. M. 2018, *MNRAS*, 477, 2716, doi: [10.1093/mnras/sty852](https://doi.org/10.1093/mnras/sty852)
- Krumholz, M. R., & McKee, C. F. 2005, *The Astrophysical Journal*, 630, 250, doi: [10.1086/431734](https://doi.org/10.1086/431734)
- Krumholz, M. R., McKee, C. F., & Bland-Hawthorn, J. 2019, *Annual Review of Astronomy and Astrophysics*, vol. 57, p.227-303, 57, 227, doi: [10.1146/annurev-astro-091918-104430](https://doi.org/10.1146/annurev-astro-091918-104430)
- Lada, C. J., & Dame, T. M. 2020, *The Astrophysical Journal*, 898, 3, doi: [10.3847/1538-4357/ab9bfb](https://doi.org/10.3847/1538-4357/ab9bfb)
- Larson, R. B. 1981, *Monthly Notices of the Royal Astronomical Society*, 194, 809, doi: [10.1093/mnras/194.4.809](https://doi.org/10.1093/mnras/194.4.809)
- Lee, E. J., Miville-Deschênes, M.-A., & Murray, N. W. 2016, *The Astrophysical Journal*, 833, 229, doi: [10.3847/1538-4357/833/2/229](https://doi.org/10.3847/1538-4357/833/2/229)
- Leitherer, C., Schaerer, D., Goldader, J. D., et al. 1999, *The Astrophysical Journal Supplement Series*, 123, 3, doi: [10.1086/313233](https://doi.org/10.1086/313233)
- Leroy, A. K., Hughes, A., Schruba, A., et al. 2016, *The Astrophysical Journal*, 831, 16, doi: [10.3847/0004-637X/831/1/16](https://doi.org/10.3847/0004-637X/831/1/16)
- Leroy, A. K., Usero, A., Schruba, A., et al. 2017, *The Astrophysical Journal*, 835, 217, doi: [10.3847/1538-4357/835/2/217](https://doi.org/10.3847/1538-4357/835/2/217)
- Leroy, A. K., Schinnerer, E., Hughes, A., et al. 2021, *ApJS*, 257, 43, doi: [10.3847/1538-4365/ac17f3](https://doi.org/10.3847/1538-4365/ac17f3)
- Li, H., Vogelsberger, M., Bryan, G. L., et al. 2022, *Monthly Notices of the Royal Astronomical Society*, 514, 265, doi: [10.1093/mnras/stac1136](https://doi.org/10.1093/mnras/stac1136)
- Li, H., Vogelsberger, M., Marinacci, F., & Gnedin, O. Y. 2019, *Monthly Notices of the Royal Astronomical Society*, 487, 364, doi: [10.1093/mnras/stz1271](https://doi.org/10.1093/mnras/stz1271)
- Martin, G., Kaviraj, S., Devriendt, J. E. G., et al. 2017, *Monthly Notices of the Royal Astronomical Society*, 472, L50, doi: [10.1093/mnrasl/slx136](https://doi.org/10.1093/mnrasl/slx136)
- McElroy, R., Bottrell, C., Hani, M. H., et al. 2022, *Monthly Notices of the Royal Astronomical Society*, 515, 3406, doi: [10.1093/mnras/stac1715](https://doi.org/10.1093/mnras/stac1715)
- McMullin, J. P., Waters, B., Schiebel, D., Young, W., & Golap, K. 2007, 376, 127
- Meidt, S. E., Leroy, A. K., Rosolowsky, E., et al. 2018, *The Astrophysical Journal*, 854, 100, doi: [10.3847/1538-4357/aaa290](https://doi.org/10.3847/1538-4357/aaa290)
- Meštrić, U., Vanzella, E., Zanella, A., et al. 2022, *Monthly Notices of the Royal Astronomical Society*, 516, 3532, doi: [10.1093/mnras/stac230910.48550/arXiv.2202.09377](https://doi.org/10.1093/mnras/stac230910.48550/arXiv.2202.09377)
- Mihos, J. C., & Hernquist, L. 1994, *The Astrophysical Journal*, 431, L9, doi: [10.1086/187460](https://doi.org/10.1086/187460)
- . 1996, *The Astrophysical Journal*, 464, 641, doi: [10.1086/177353](https://doi.org/10.1086/177353)
- Miville-Deschênes, M.-A., Murray, N., & Lee, E. J. 2017, *The Astrophysical Journal*, 834, 57, doi: [10.3847/1538-4357/834/1/57](https://doi.org/10.3847/1538-4357/834/1/57)
- Mocz, P., & Burkhardt, B. 2018, *MNRAS*, 480, 3916, doi: [10.1093/mnras/sty1976](https://doi.org/10.1093/mnras/sty1976)
- Moreno, J., Torrey, P., Ellison, S. L., et al. 2015, *Monthly Notices of the Royal Astronomical Society*, 448, 1107, doi: [10.1093/mnras/stv094](https://doi.org/10.1093/mnras/stv094)
- . 2019, *Monthly Notices of the Royal Astronomical Society*, 485, 1320, doi: [10.1093/mnras/stz417](https://doi.org/10.1093/mnras/stz417)
- . 2021, *Monthly Notices of the Royal Astronomical Society*, 503, 3113, doi: [10.1093/mnras/staa2952](https://doi.org/10.1093/mnras/staa2952)
- Muraoka, K., Kohno, K., Tosaki, T., et al. 2009, *The Astrophysical Journal*, 706, 1213, doi: [10.1088/0004-637X/706/2/1213](https://doi.org/10.1088/0004-637X/706/2/1213)
- Murray, N., Quataert, E., & Thompson, T. A. 2010, *The Astrophysical Journal*, 709, 191, doi: [10.1088/0004-637X/709/1/191](https://doi.org/10.1088/0004-637X/709/1/191)
- Mutch, S. J., Croton, D. J., & Poole, G. B. 2011, *The Astrophysical Journal*, 736, 84, doi: [10.1088/0004-637X/736/2/84](https://doi.org/10.1088/0004-637X/736/2/84)
- Myers, A. T., Klein, R. I., Krumholz, M. R., & McKee, C. F. 2014, *Monthly Notices of the Royal Astronomical Society*, 439, 3420, doi: [10.1093/mnras/stu190](https://doi.org/10.1093/mnras/stu190)

- Narayanan, D., Krumholz, M., Ostriker, E. C., & Hernquist, L. 2011, *Monthly Notices of the Royal Astronomical Society*, 418, 664, doi: [10.1111/j.1365-2966.2011.19516.x](https://doi.org/10.1111/j.1365-2966.2011.19516.x)
- Nieten, C., Neininger, N., Guélin, M., et al. 2006, *Astronomy and Astrophysics*, Volume 453, Issue 2, July II 2006, pp.459-475, 453, 459, doi: [10.1051/0004-6361/20035672](https://doi.org/10.1051/0004-6361/20035672)
- Orr, M. E., Hayward, C. C., Hopkins, P. F., et al. 2018, *Monthly Notices of the Royal Astronomical Society*, 478, 3653, doi: [10.1093/mnras/sty1241](https://doi.org/10.1093/mnras/sty1241)
- Orr, M. E., Hatchfield, H. P., Battersby, C., et al. 2021, *The Astrophysical Journal*, 908, L31, doi: [10.3847/2041-8213/abdebd](https://doi.org/10.3847/2041-8213/abdebd)
- Papadopoulos, P. P., van der Werf, P. P., Xilouris, E. M., et al. 2012, *Monthly Notices of the Royal Astronomical Society*, 426, 2601, doi: [10.1111/j.1365-2966.2012.21001.x](https://doi.org/10.1111/j.1365-2966.2012.21001.x)
- Patton, D. R., Torrey, P., Ellison, S. L., Mendel, J. T., & Scudder, J. M. 2013, *Monthly Notices of the Royal Astronomical Society*, 433, L59, doi: [10.1093/mnras/slt058](https://doi.org/10.1093/mnras/slt058)
- Patton, D. R., Wilson, K. D., Metrow, C. J., et al. 2020, *Monthly Notices of the Royal Astronomical Society*, 494, 4969, doi: [10.1093/mnras/staa913](https://doi.org/10.1093/mnras/staa913)
- Privon, G. C., Barnes, J. E., Evans, A. S., et al. 2013, *Astrophysical Journal*, 771, doi: [10.1088/0004-637X/771/2/120](https://doi.org/10.1088/0004-637X/771/2/120)
- Raskutti, S., Ostriker, E. C., & Skinner, M. A. 2016, *The Astrophysical Journal*, 829, 130, doi: [10.3847/0004-637X/829/2/130](https://doi.org/10.3847/0004-637X/829/2/130)
- Renaud, F., Boily, C. M., Naab, T., & Theis, C. 2009, *Astrophysical Journal*, 706, 67, doi: [10.1088/0004-637X/706/1/67](https://doi.org/10.1088/0004-637X/706/1/67)
- Renaud, F., Bournaud, F., Agertz, O., et al. 2019a, *Astronomy & Astrophysics*, 625, A65, doi: [10.1051/0004-6361/201935222](https://doi.org/10.1051/0004-6361/201935222)
- Renaud, F., Bournaud, F., Daddi, E., & Weiß, A. 2019b, *Astronomy & Astrophysics*, Volume 621, id.A104, <NUMPAGES>5</NUMPAGES> pp., 621, A104, doi: [10.1051/0004-6361/201834397](https://doi.org/10.1051/0004-6361/201834397)
- Renaud, F., Bournaud, F., Kraljic, K., & Duc, P. A. 2014, *Monthly Notices of the Royal Astronomical Society: Letters*, 442, doi: [10.1093/mnrasl/slu050](https://doi.org/10.1093/mnrasl/slu050)
- Rey, M. P., Agertz, O., Starkenburg, T. K., et al. 2022, *VINTERGATAN-GM: The Cosmological Imprints of Early Mergers on Milky-Way-mass Galaxies*
- Rice, T. S., Goodman, A. A., Bergin, E. A., Beaumont, C., & Dame, T. M. 2016, *The Astrophysical Journal*, 822, 52, doi: [10.3847/0004-637X/822/1/52](https://doi.org/10.3847/0004-637X/822/1/52)
- Rico-Villas, F., Martin-Pintado, J., Gonzalez-Alfonso, E., Martin, S., & Rivilla, V. M. 2020, *Monthly Notices of the Royal Astronomical Society*, 491, 4573, doi: [10.1093/mnras/stz3347](https://doi.org/10.1093/mnras/stz3347)
- Robertson, B., Bullock, J. S., Cox, T. J., et al. 2006, *The Astrophysical Journal*, 645, 986, doi: [10.1086/504412](https://doi.org/10.1086/504412)
- Rodríguez Montero, F., Davé, R., Wild, V., Anglés-Alcázar, D., & Narayanan, D. 2019, *Monthly Notices of the Royal Astronomical Society*, 490, 2139, doi: [10.1093/mnras/stz2580](https://doi.org/10.1093/mnras/stz2580)
- Roman-Duval, J., Jackson, J. M., Heyer, M., Rathborne, J., & Simon, R. 2010, *The Astrophysical Journal*, 723, 492, doi: [10.1088/0004-637X/723/1/492](https://doi.org/10.1088/0004-637X/723/1/492)
- Rosolowsky, E., Hughes, A., Leroy, A. K., et al. 2021, *Monthly Notices of the Royal Astronomical Society*, 502, 1218, doi: [10.1093/mnras/stab085](https://doi.org/10.1093/mnras/stab085)
- Saintonge, A., Catinella, B., Tacconi, L. J., et al. 2017, *The Astrophysical Journal Supplement Series*, 233, 22, doi: [10.3847/1538-4365/aa97e0](https://doi.org/10.3847/1538-4365/aa97e0)
- Sakamoto, K., Aalto, S., Combes, F., Evans, A., & Peck, A. 2014, *The Astrophysical Journal*, 797, 90, doi: [10.1088/0004-637X/797/2/90](https://doi.org/10.1088/0004-637X/797/2/90)
- Sánchez-García, M., Pereira-Santaella, M., García-Burillo, S., et al. 2022, *Astronomy & Astrophysics*, Volume 659, id.A102, <NUMPAGES>20</NUMPAGES> pp., 659, A102, doi: [10.1051/0004-6361/202141963](https://doi.org/10.1051/0004-6361/202141963)
- Sargent, M. T., Daddi, E., Béthermin, M., et al. 2014, *Astrophysical Journal*, 793, doi: [10.1088/0004-637X/793/1/19](https://doi.org/10.1088/0004-637X/793/1/19)
- Sawala, T., Frenk, C. S., Fattahi, A., et al. 2014, *Local Group Galaxies Emerge from the Dark*
- Schirm, M. R. P., Wilson, C. D., Parkin, T. J., et al. 2014, *The Astrophysical Journal*, 781, 101, doi: [10.1088/0004-637X/781/2/101](https://doi.org/10.1088/0004-637X/781/2/101)
- Schruba, A., Kruijssen, J. M. D., & Leroy, A. K. 2019, *The Astrophysical Journal*, 883, 2, doi: [10.3847/1538-4357/ab3a43](https://doi.org/10.3847/1538-4357/ab3a43)
- Scudder, J. M., Ellison, S. L., Momjian, E., et al. 2015, *Monthly Notices of the Royal Astronomical Society*, 449, 3719, doi: [10.1093/mnras/stv588](https://doi.org/10.1093/mnras/stv588)
- Seillé, L. M., Buat, V., Haddad, W., et al. 2022, *Spatial Disconnection between Stellar and Dust Emissions: The Test of the Antennae Galaxies (Arp 244)*
- Sick, J., Courteau, S., Cuillandre, J.-C., et al. 2015, 311, 82, doi: [10.1017/S1743921315003440](https://doi.org/10.1017/S1743921315003440)
- Smith, M. C., Bryan, G. L., Somerville, R. S., et al. 2021, *Monthly Notices of the Royal Astronomical Society*, 506, 3882, doi: [10.1093/mnras/stab1896](https://doi.org/10.1093/mnras/stab1896)

- Sun, J., Leroy, A. K., Schruba, A., et al. 2018, *The Astrophysical Journal*, 860, 172, doi: [10.3847/1538-4357/aac326](https://doi.org/10.3847/1538-4357/aac326)
- Sun, J., Leroy, A. K., Schinnerer, E., et al. 2020, *ApJL*, 901, L8, doi: [10.3847/2041-8213/abb3be](https://doi.org/10.3847/2041-8213/abb3be)
- Sun, J., Leroy, A. K., Rosolowsky, E., et al. 2022, *The Astronomical Journal*, 164, 43, doi: [10.3847/1538-3881/ac74bd](https://doi.org/10.3847/1538-3881/ac74bd)
- Teyssier, R., Chapon, D., & Bournaud, F. 2010, *Astrophysical Journal Letters*, 720, 149, doi: [10.1088/2041-8205/720/2/L149](https://doi.org/10.1088/2041-8205/720/2/L149)
- Thorp, M. D., Ellison, S. L., Pan, H.-A., et al. 2022, *Monthly Notices of the Royal Astronomical Society*, 516, 1462, doi: [10.1093/mnras/stac2288](https://doi.org/10.1093/mnras/stac2288)
- Tosaki, T., Kohno, K., Harada, N., et al. 2017, *Publications of the Astronomical Society of Japan*, 69, 18, doi: [10.1093/pasj/psw122](https://doi.org/10.1093/pasj/psw122)
- Ueda, J., Iono, D., Petitpas, G., et al. 2012, *The Astrophysical Journal*, 745, 65, doi: [10.1088/0004-637X/745/1/65](https://doi.org/10.1088/0004-637X/745/1/65)
- Wei, L. H., Keto, E., & Ho, L. C. 2012, *The Astrophysical Journal*, 750, 136, doi: [10.1088/0004-637X/750/2/136](https://doi.org/10.1088/0004-637X/750/2/136)
- Whitmore, B. C., Brogan, C., Chandar, R., et al. 2014, *ApJ*, 795, 156, doi: [10.1088/0004-637X/795/2/156](https://doi.org/10.1088/0004-637X/795/2/156)
- Wilson, C. D., Elmegreen, B. G., Bemis, A., & Brunetti, N. 2019, *The Astrophysical Journal*, 882, 5, doi: [10.3847/1538-4357/ab31f3](https://doi.org/10.3847/1538-4357/ab31f3)
- Wilson, C. D., Scoville, N., Madden, S. C., & Charmandaris, V. 2000, *The Astrophysical Journal*, 542, 120, doi: [10.1086/309504](https://doi.org/10.1086/309504)
- Zhang, Q., Fall, S. M., & Whitmore, B. C. 2001, *Observatory*, 10
- Zhu, M., Seaquist, E. R., & Kuno, N. 2003, *The Astrophysical Journal*, 588, 243, doi: [10.1086/368353](https://doi.org/10.1086/368353)

APPENDIX

A. INFLUENCE FROM DIFFERENT VIEWING ANGLES

One important factor that might influence Σ_{mol} measured from the simulations is the inclination angle at which the galaxy is viewed. For the simulated control galaxies, we pick the inclination angle of 30 degrees in Fig. 1. By increasing inclination angle we might see significant increase in Σ_{mol} . Fig. A1 shows the data for the G3 galaxy viewed with inclination angles of 30, 60 and 80 degrees. We see little increase in Σ_{mol} even for an inclination of 80 degrees. This is consistent with our expectation that individual clouds are resolved in the simulated data. For resolved spherical clouds, the observed surface density should always be the same despite different viewing angles.

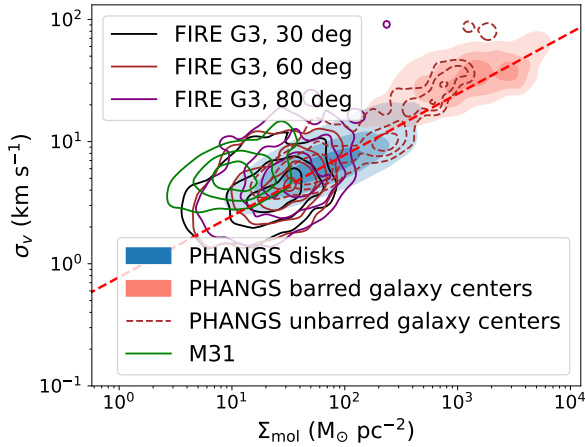


Figure A1. Similar to Fig. 1 but with the simulated G3 galaxy viewed at different inclination angles (30, 60 and 80 degrees).

For the simulated mergers, the molecular gas structure is more complicated than a single layer of gas disk. In this case, we might pick a specific angle where multiple clouds happen to lie along the same line of sight, which gives us large σ_v values. To test if this is the actual case, we examine a snapshot at 2.87 when we reach maximal Σ_{mol} and σ_v from a different angle ('v1'). As shown in Fig. A2, we see similar gas distribution contour in σ_v vs Σ_{mol} contour. This along with the velocity spectrum in Fig. 6 suggests that the large σ_v and α_{vir} we measured is intrinsic properties of individual GMCs.

B. GLOBAL GAS FRACTION

On global scales, we compare the molecular gas mass and total gas mass (including HI) of the FIRE-2 galax-

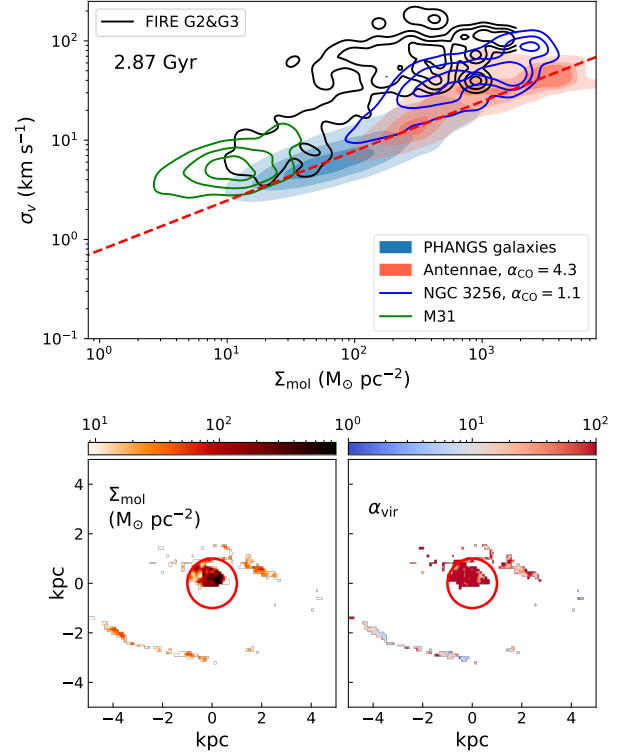


Figure A2. The snapshot of FIRE-2 merger at a time of 2.87 Gyr with viewing angles of 'v1', which is roughly perpendicular (with an angle of 109 degree) to the 'v0' angle. (Upper) the σ_v vs Σ_{mol} distribution of GMCs. (Lower) The Σ_{mol} map of the snapshot. We can see that viewing from different angles still give us high σ_v measurement, which also suggests that σ_v we measure is not the velocity dispersion among GMCs along the line of sight. (lower) The Σ_{mol} and σ_v for this snapshot from 'v1' angle.

ies with observed values for normal spiral galaxies. We compare to both the PHANGS galaxies (Leroy et al. 2021) as well as to the global gas properties from the xCOLDGASS survey, to confirm that the PHANGS galaxies are representative of star forming main sequence galaxies in our local universe. For xCOLDGASS, the molecular gas mass is extracted from Saintonge et al. (2017) and the total gas mass is from Catinella et al. (2018).

In interpreting the lower Σ_{mol} values seen in Fig. 1, one possibility is that there may not be as much gas available to form high surface density clouds in the two simulated galaxies compared to the PHANGS galaxies. Fig. B1 compares the global molecular gas masses, M_{mol} , and molecular gas fractions, $f_{\text{mol}} = M_{\text{mol}} / M_{\star}$, for the FIRE-2 mergers with those of the PHANGS

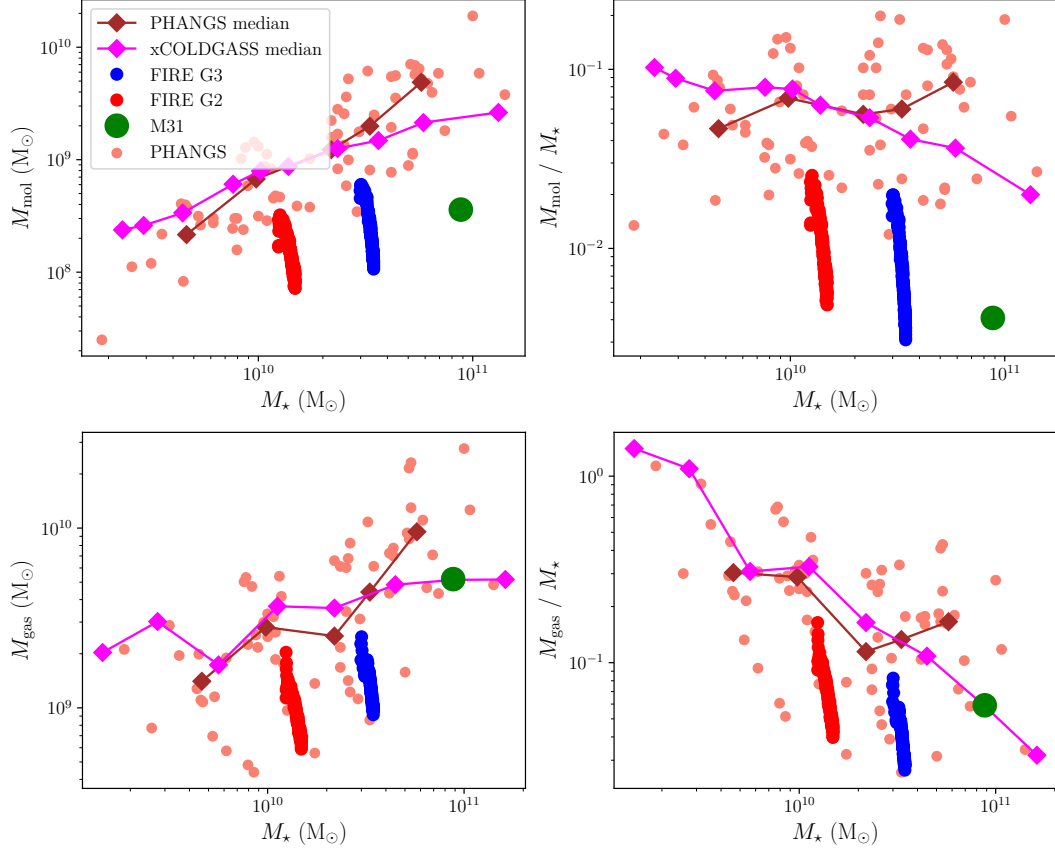


Figure B1. (Upper Left) M_{mol} versus M_{\star} for PHANGS galaxies (salmon dots; Leroy et al. 2021), M 31 (green filled circle; Nieten et al. 2006) and the G2 (red points) and G3 (blue points) simulated galaxies at different times in their evolution. Note that the G2 and G3 simulated galaxies lie significantly below the star-forming main sequence defined by the xCOLDGASS sample. (Upper Right) f_{mol} versus M_{\star} for the same galaxies. The molecular gas fractions of G2 and G3 are significantly lower than most of the PHANGS spiral galaxies. (Lower left) total gas versus M_{\star} . (Lower right) total gas fraction versus M_{\star} . These comparisons suggest that the low Σ_{mol} measured for the simulated galaxies might be due to the low total and molecular gas fraction in the initial set-up.

galaxies from Sun et al. (2020). We also show the median value of M_{mol} and f_{gas} in each M_{\star} bin for the PHANGS galaxies, as well as the weighted median of M_{\star} and f_{mol} for galaxies in xCOLDGASS sample (Saintonge et al. 2017). The two median values are quite close to each other for galaxies with M_{\star} of $10^{9.5} - 10^{11} M_{\odot}$, although the PHANGS galaxies seem to deviate somewhat from the xCOLDGASS sample in the highest and lowest mass bins. In contrast, the G2 and G3 galaxies both have $f_{\text{mol}} \sim 3$ times lower than typical PHANGS or xCOLDGASS galaxies of the same stellar mass. Therefore, the small global f_{mol} may be responsible for producing the low Σ_{mol} values seen in the simulated galaxies.

The low values of f_{mol} could be produced either by the initial set-up of the simulations or by physical mechanisms in the simulation that lead to inefficient conversion of gas into the cold phase. We can distinguish between these two options by calculating the total gas fraction

f_{gas} including both HI and H₂. The lower panel of Fig. B1 shows the median of M_{gas} and f_{gas} for the PHANGS galaxies and xGASS-CO samples (Catinella et al. 2018) compared to the two simulated galaxies. The values of f_{gas} for both simulated galaxies are still ~ 3 times lower than those of typical spiral galaxies with similar M_{\star} . Therefore, it seems most likely that the low cold gas fraction, f_{mol} , is produced by a low total (cold+warm+hot) gas mass in the initial set-up of the simulations.

C. SNAPSHOTS FOR ‘E1’ ORBIT

Here we show the SFR history and 3 example snapshots for G2&G3 ‘e1’ orbit in Fig. C1.

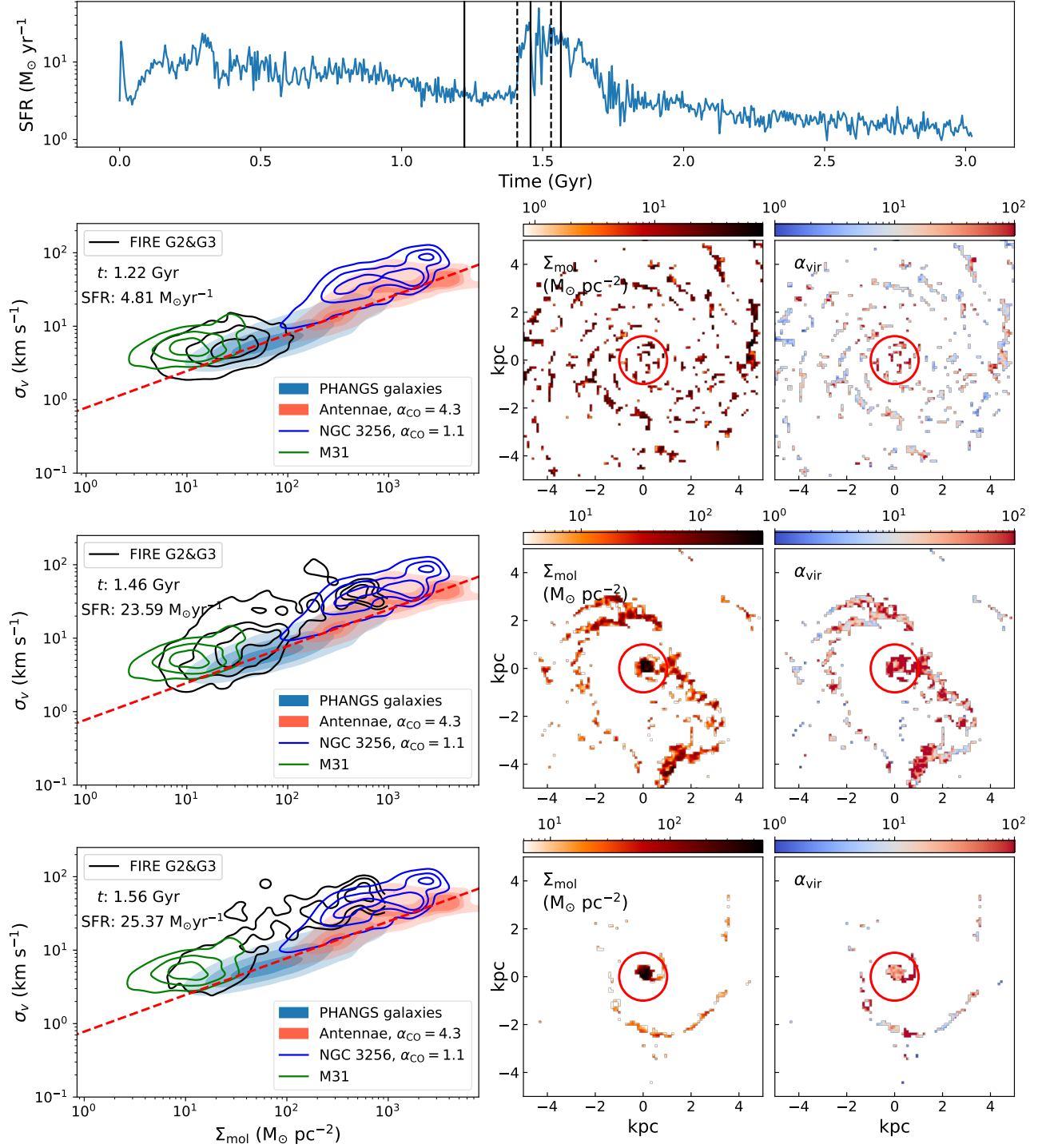


Figure C1. Similar plot as Figure 2 but with SFR history and 3 snapshots from ‘e1’ orbit. The interactive version of the animation is available at https://htmlpreview.github.io/?https://github.com/heh15/merger_animations/blob/main/G2G3_e1_v0.html